Characterization Of A New Sapphire Microstrip Detector to be used as a Gamma Beam Profiler in The LUXE Experiment at DESY

Master Degree in Physics of Matter

Candidate:

Salman Aboud

(Student ID: 2004984)

Thesis supervisor: Dr. Mauro Morandin

Thesis co-supervisor: Pietro Grutta

Abstract

   LUXE (Laser Und XFEL Experiment) aims to study strong-field Quantum Electro-dynamics (SFQED) processes by: (1) observing Sauter-Schwinger pair production; (2) investigating the SFQED transition in non-linear (inverse) Compton scattering (ICS), Breit-Wheeler production, and the trident process; (3) exploring natural models of axion-like particles (ALPs) coupling to photons (γs). Two main set-ups are being investigated in LUXE using the European XFEL: (1) the direct collision of the electron (e^-) beam with a high-power laser ($e^- -$ laser setup) ; (2) the conversion of e^- beam to a γ beam before interaction with the laser (γ-laser setup). In a $e^- -$ laser setup run, e^- rest-frame field is Lorentz-boosted exceeding the Schwinger limit allowing access to SFQED phenomena.

To characterize this interaction, a measurement of the laser intensity is performed by measuring the angular distribution of the Compton γs. Hence, this measurement of the gamma profile indirectly estimates the laser pulse intensity. For such collisions with high radiation doses, the detector should have a radiation-hard material (up to 10 MGy) and a resolution (of $5 \ \mu\text{m}$). Therefore, a sapphire microstrip detector is proposed for such a task: the gamma beam profiler (GBP).

The development, characterization, and optimization of the sapphire micro-strip detector as a GBP for LUXE are explored using a two-pronged approach. The first approach is a Monte Carlo (MC) simulation to replicate the GBP's performance under various SFQED interactions within LUXE. This simulation provides energy deposition maps, serving as input for a custom digitization MC simulation, which simulates charge collection, front-end response and ADC conversion. This process is crucial for reconstructing the gamma beam profile, measuring beam width resolution and optimizing the performance of GBP. The second approach involves experimental testing (at CLEAR-CERN) and characterization of the GBP from prototypes.

Contents

Introduction

LUXE, also known as the Laser Und XFEL experiment, is a novel scientific project being planned at DESY Hamburg. It utilizes the electron beam of the European XFEL with the primary goal of studying non-perturbative Quantum Electrodynamics (QED) in exceptionally strong fields (comparable to or exceeding the Schwinger critical field) [1]. The study of this unexplored regime is achieved through the interaction of an ultra-high intensity laser with 16.5 GeV electrons from the XFEL electron beam [2].

In its scientific endeavor, LUXE [1] is primarily focused on two pivotal objectives within the realm of physics. The first objective is to conduct precise measurements that are instrumental in probing the shift into the non-perturbative regime of QED, commonly referred to as strong-field QED (SFQED). This transition represents a critical juncture where the perturbative approach, traditionally reliant on the expansion of interacting theories around free solutions, becomes insufficient. In QED, which is a field theory that governs the interactions of fermions and photons, the perturbative expansion is contingent upon a coupling constant. This constant, known as the fine structure constant, inherently varies with the energy scale of the experiments conducted. The specific perturbative regime of interest here is linked to a modulation in this constant induced by the interaction of fermions with an external (semi-classical) electromagnetic field. This interaction causes the coupling constant to be influenced by the settings of the electromagnetic field within the laboratory. Consequently, adjusting these settings might lead to a regime wherein expanding solutions around minimal values of the external field becomes untenable.

The second objective of LUXE is to explore the possibility of new particle phenomena that interact with photons, extending beyond the Standard Model. In pursuit of this goal, LUXE will measure the interactions between real photons and electrons, as well as between photons themselves, at field strengths where these interactions become non-perturbative. This involves transitioning from a regime where the perturbative approach is valid to one where it is not, within the

context of QED. Furthermore, LUXE will leverage SFQED processes as a means to innovatively search for new particles beyond the Standard Model, particularly those that exhibit coupling with photons. The intricate physics underpinning the LUXE experiment, along with its comprehensive scientific rationale, will be elaborated in Chapter 2.

To achieve these objectives, LUXE will use the high-quality European XFEL electron-beam and a high-power laser (40 TW in phase0, up to XTW in phase1), along with sophisticated diagnostics and a detection system. In the context of this thesis, the detector for gamma beams was tested at CERN Linear Electron Accelerator for Research (CLEAR) as it will be discussed further in Chapter 5.

LUXE will employ two configurations to achieve its objectives. In the first configuration, the Eu.XFEL $16.5 \, \text{GeV}$ electron beam will be directed through the focus of a high-intensity laser. In the second configuration, a high-energy photon beam generated during the propagation of the electron beam through a high-Z solid target will interact with the focus of a high-intensity laser [3]. LUXE expriment and its set-ups will be discussed in details in Chapter 2.

A key component of this experiment is the Gamma Beam Profiler (GBP). The GBP is a novel Sapphire detector, which is central to measuring the transverse beam profiles [2]. The GBP's development and optimization are significant aspects of the research and development phase of LUXE, given its crucial role in providing important data on the spatial distribution of the gamma-ray photons produced during the experiment. This information is essential to understand the quality of the interactions. The characterization and optimization of the GBP is studied and explained further throughout the thesis.

The aforementioned implementation relies on the MC simulation of GBP in order to optimize the digitization parameters of the detectors, this will be discussed in Chapter 4 and 6.

The LUXE experiment at DESY

2.1 Scientific Motivation

Quantum Electrodynamics (QED) has been a fundamental framework in modern physics since its establishment by Paul Dirac in 1927 [4]. It has significantly contributed to understanding the interactions between light and matter by combining principles from both quantum mechanics and special relativity.

The foundational premise of QED is the mediation of electromagnetic interactions through the exchange of virtual photons. Although not directly observable, the impact of these virtual particles is measurable and predictable, thereby providing a robust mathematical framework to explain phenomena involving electrically charged particles interacting through photon exchange [5].

In QED, the natural constants of the theory, such as the electron charge e and mass m_e, lead to the definition of a characteristic electric field scale known as the Schwinger Limit. This limit is mathematically expressed as

$$E_{\mathrm{cr}} = \frac{m^2 c^3}{e\hbar} = 1.32 \times 10^{18}\,\mathrm{Vcm}^{-1}.$$

It serves as a benchmark for defining what constitutes a 'strong' electromagnetic (EM) field in QED, particularly in comparison to this Schwinger Limit.

However, the experimental pursuit of reaching or approaching such high field values presents significant challenges. The Schwinger Limit is substantially higher than any EM field strength that can be currently produced in laboratory settings. Despite these limitations, the exploration of strong EM fields within the framework of QED is of considerable interest. In systems characterized by weak EM fields, QED has been rigorously tested and validated. Notable examples include precision

measurements of the electron's anomalous magnetic moment [6], atomic hyper-fine splitting, and the Lamb shift, all of which conform to QED predictions with remarkable accuracy, aligning with the fine structure constant α to approximately 81 parts per trillion [7] [8]. Nonetheless, in the realm of strong EM fields, QED forecasts phenomena that still await experimental confirmation.

Henceforth, in the rest frame of a high-energy probe charge, the EM field strength E is enhanced by the Lorentz factor, γ, to $E^* = \gamma E(1 + \cos\theta)$, where θ is the angle between the momenta of the electron beam and laser pluses. In LUXE setup, the angle is $\theta = 17.2$ degrees. By arranging a collision between the 16.5 GeV XFEL.EU electron beam and intense laser pulses generated by the laser, the electron rest-frame field at LUXE can overcome the Schwinger Limit, thus enabling access to strong-field QED phenomena.

QED in intense EM fields [9] manifests in a variety of settings. In astrophysics, pair creation associated with the gravitational collapse of black holes [10], the propagation of cosmic rays [11] are noteworthy, some neutron stars, possessing strong magnetization, have magnetospheres that probe the Schwinger limit [12–14]. In particle physics, beam-beam collisions at future high-energy lepton colliders are anticipated to exhibit strong-field effects prominently [15, 16], and the probing of the Coulomb field of heavy ions can be sensitive to strong-field effects [17]. Albeit in non-relativistic systems where the field strength scale is determined by the ionization potential, strong fields are a significant area of investigation within the atomic and molecular physics communities [18].

In a plane wave EM background, this coupling is characterized by the classical nonlinearity parameter $\xi = \frac{|e|E\lambda_e}{\hbar\omega_L}$, representing the work done by the EM field over a Compton wavelength in units of the EM field photon energy ($|e|$ is the elementary charge, λ_e the reduced Compton wavelength of an electron, and $\hbar\omega_L$ the energy of a background photon). The ξ parameter quantifies the interaction of multiple laser photons with the charge in a given QED process, with the probability of n background photons scaling as $\sim \xi^{2n}$.

In weak fields, the probabilities of QED events scale as $\sim \xi^2$, with higher-order interactions with respect to the background being suppressed. However, when $\xi \sim O(1)$, this perturbative hierarchy ceases to exist, necessitating the consideration of all interactions between the charge and laser background. In sufficiently strong fields, the probability of QED processes exhibits a non-perturbative dependency on the EM field. This parameter, occasionally referred to as the 'intensity parameter', can be expressed as $\xi = \sqrt{\frac{I_L}{I_{cr}}\left(\frac{m_e c^2}{\hbar\omega_L}\right)}$, where $\frac{I_L}{I_{cr}}$ is the ratio of the laser

intensity to the intensity of a field at the Schwinger limit and m_e is the electron mass.

Therefore, the primary objectives of the LUXE experiment encompass:

1 Evaluating the interactions of actual photons with electrons and positrons at field strengths where the coupling to charges is in non-perturbative regime;

2 Conducting precise measurements of electron-photon and photon-photon interactions during the transition from the perturbative to the non-perturbative regime of quantum electrodynamics (QED);

3 Employing strong-field QED processes to make a sensitive search for new particles beyond the Standard Model that couple to photons.

2.2 Physics of LUXE

2.2.1 Theory background

QED stands as a pinnacle of precision in our understanding of nature. Experiments that delve into the intricacies of QED, such as the electron's anomalous magnetic moment (often referred to as "$(g2)_e$"), have showcased an unparalleled harmony between theoretical predictions and experimental outcomes. This harmony is attributed to the weak coupling nature of QED at the relevant energy scales. Essentially, this means that we can obtain highly accurate theoretical predictions by expanding in terms of the small QED coupling, given by

$$\alpha \equiv \frac{e^2}{4\pi c} \simeq \frac{1}{137} \qquad \text{2.1}$$

where we've normalized the vacuum's permittivity to one. It is important to distinguish between the perturbative expansion of processes in QED and the quantum corrections (loops) that contribute to the electron's anomalous magnetic moment. The perturbative expansion of QED processes, including the electron's magnetic moment, involves expressing physical quantities as a power series in α. The theoretical computation of the electron's anomalous magnetic moment, incorporating quantum loop corrections, has been carried out to high precision. These calculations, up to the fifth order in α, have led to theoretical predictions that align with experimental observations to a remarkable degree, achieving an accuracy better than 1 part per billion (ppb) [6]. This precision is a proof of the strength of QED as a predictive framework and its ability to account for complex quantum phenomena.

However, there is a phenomenon known as vacuum polarization that causes the charge, and consequently the coupling α, to vary with energy or spatial resolution. At extremely high energies, approaching the 'Landau pole' [19], the running coupling α grows indefinitely, making the perturbative approach untenable. This suggests that QED might need to be replaced or augmented by a more foundational theory, often referred as its ultraviolet completion [20]. This challenge persists even when considering QED as a subset of the electroweak component of the Standard Model. In this context, the Landau pole issue is significantly reduced but still remains well beyond the Planck energy of 10^{19} GeV. To make it clear, the landau pole is an issue because it signals that QED theory is incomplete but it is not an issue because these energies are completely unreachable.

Given the inaccessibility of energies near the Landau pole, it's pertinent to ask if there are alternative methods to probe the non-perturbative domain of QED. One strategy involves leveraging an external field to effectively amplify the coupling. If this external field is sufficiently intense, the effective coupling might approach unity. But what qualifies as an "intense" field in the realm of QED? A typical field strength in QED can be deduced via dimensional analysis, leading to the renowned Schwinger limit E_{cr}. Achieving such a field strength over the characteristic distance of an electron's Compton wavelength, approximately 400 fm, is a formidable challenge. One approach involves leveraging the Coulomb field of heavy nuclei, which can effectively scale up the coupling by a factor of $Z\alpha$, where Z is the atomic number. However, high-Z systems come with their own set of challenges, primarily the difficulty of distinguishing QED effects from nuclear or strong interaction effects, which are inherently non-perturbative. One notable exception is the scenario of ultra-peripheral collisions (UPCs) at high energies, where fields approaching the Schwinger limit might be achievable in laboratory settings [10].

In recent times, advancements in laser technology have opened up new avenues to generate ultra-intense electromagnetic fields in a controlled environment [21] [22]. The LUXE experiment aims to harness these fields to study strong-field QED processes, such as non-linear Compton scattering, Breit-Wheeler pair creation and the non-linear trident process. (A table of these processes is given in Fig. 2.1). A key parameter in these studies is the classical non-linearity parameter ξ, which quantifies the non-linearity of the interaction between the laser field and charged particles. When ξ is of the order of unity, it signifies a transition from the perturbative to the non-perturbative regime of QED.

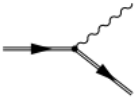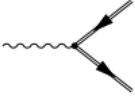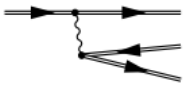**FIGURE 2.1** • Physical processes for the LUXE. Double lines indicate fermions in a laser background.

The quantum non-linearity parameter, denoted by χ, measures the importance of quantum effects in the interaction. In certain conditions, when χ is sufficiently large, radiative corrections can dominate, leading to a distinct type of non-perturbativity in strong-field QED [23]. For convenience, the relevant parameters introduced so far are reported in the table Tab. 2.1, with the typical range accessed by LUXE. For the benefit of easier reading of this thesis, Tab. 2.2 presents the meaning of some of the commonly used symbols.

	Theory Parameter	Definition	Range accessed in LUXE phase-0	phase-1
ξ	Classical non-linearity parameter	$\xi = \dfrac{m_e}{\omega_L}\dfrac{\mathscr{E}_{\mathrm{L}}}{\mathscr{E}_{\mathrm{cr}}}$	≤ 6	≤ 19
η_i	Energy parameter	$\eta_i = \dfrac{\omega_L \varepsilon_i}{m_e^2}(1+\beta\cos\theta)$	$\eta_i \leq 0.2$	
χ_i	Quantum non-linearity parameter	$\chi_i = \dfrac{\varepsilon_i}{m_e}\dfrac{\mathscr{E}_{\mathrm{L}}}{\mathscr{E}_{\mathrm{cr}}}(1+\beta\cos\theta)$	≤ 1	≤ 3

TABLE 2.1 • Table of LUXE Parameters. Here, m_e is the electron mass, ω_L is the laser frequency, ε represents the energy of the particle (electron, positron, photon), and θ denotes the collision angle of the particle with the laser pulse. When $\theta = 0$, the collision is "head-on". $\mathscr{E}_L$ is the instantaneous laser field strength, $\mathscr{E}_{\mathrm{cr}}$ is the Schwinger limit, and m_e is the electron mass. The relation $\hbar = c = 1$ has been used, with $\beta = 1$ for photons and $\beta \approx 1$ for electrons.

Symbol	Description
e^-	Electron
e^+	Positron
γ_L	Laser photon
γ_B	Bremsstrahlung photon
γ_C	Inverse Compton Scattered photon
γ	Radiated photon

TABLE 2.2 • Table of commonly-used symbols.

Beyond the realm of QED, there are compelling reasons, both experimental and theoretical, to believe in the existence of new physics beyond the Standard Model (SM). Phenomena like neutrino oscillations and the absence of a viable dark matter candidate within the SM framework hint at this [14] [24]. The LUXE experiment, with its ability to generate a high energy, strongly collimated, intense gamma beam", might also offer insights into beyond the Standard Model (BSM) physics, potentially shedding light on new particles or interactions.

The plane wave model

The LUXE experiment employs a focused laser pulse to establish a strong electromagnetic field. Given the absence of exact analytical solutions to the Dirac equation within this context, solutions are evaluated numerically. This relies on approximation of the field dynamics and its interaction with the background EM field. The simplest approximation is the 'plane wave model', which relies on the assumptions:

1 The intense laser pulse field's back reaction and depletion are negligible, allowing its approximation as a classical background.

2 Particles, when accelerated by strong EM fields, exhibit high relativistic behaviors. In the rest frame of these particles, any EM background closely resembles a plane wave pulse.

In a classical plane-wave field, solutions to the Dirac equation are identifiable, leading to the derivation of the Volkov solutions [25]. Using these solutions, scattering processes are computed perturbatively. This approach facilitates the extension of standard QED's Feynman rules to a plane wave setting. The calculations for processes are executed for individual probe particles, including electrons, positrons, and photons.
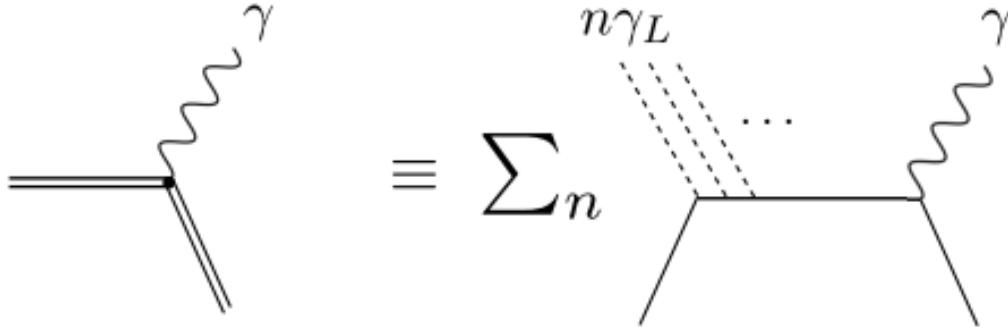
Nonlinear Compton Process

FIGURE 2.2 • The nonlinear Compton process. **Left:** a dressed electron in the laser background (double solid lines) emits a single high energy photon, γ. **Right:** a sum of Compton processes where the electron interacts with n laser photons γ_L (dashed lines), and emits a single high energy photon.

A central process under examination in the LUXE experiment is nonlinear (inverse) Compton (NLC) scattering. In this process, an electron/positron absorbs n optical photons, denoted as γ_L, from the laser background and transforms them into a singular high-energy gamma photon:

$$e^\pm + n\gamma_L \rightarrow e^\pm + \gamma. \tag{2.2}$$

This process has classical limit. The degree to which QED diverges from this classical limit is partially encapsulated by the 'quantum non-linearity parameter', χ, representing the ratio of the laser EM field to the Schwinger limit, in the electron's rest frame.

The magnitude of nonlinear and quantum effects is prominently manifested at the 'Compton edge' [26] in electron and photon spectra.
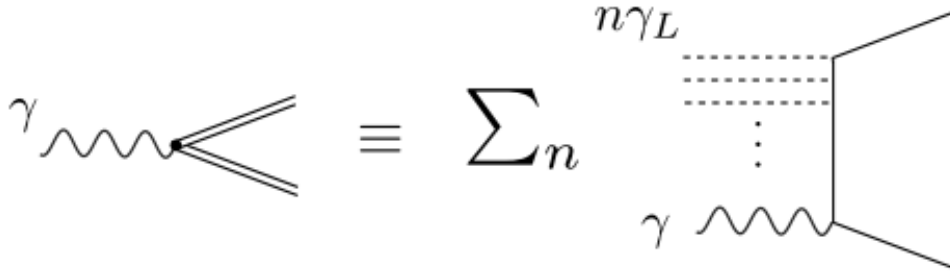
Breit-Wheeler Process

FIGURE 2.3 • The nonlinear Breit-Wheeler process. **Left:** a high energy photon γ produces an electron-positron pair that is dressed in the laser background (double solid lines). **Right:** a sum of Breit-Wheeler processes involving n laser photons γ_L (dashed lines).

The Breit-Wheeler process, shown in Fig. 2.3 pertains to the phenomenon where a photon produces an electron-positron pair in the presence of a laser pulse. In the LUXE experiment, this process will be probed in the gamma-laser setup.

For $\xi^2 \ll 1$, the Breit-Wheeler process follows a perturbative approach, known as the "multiphoton" process, with a probability scaling as $P \propto \xi^{2n^*}$. This behavior is showcased in Fig. 2.4.
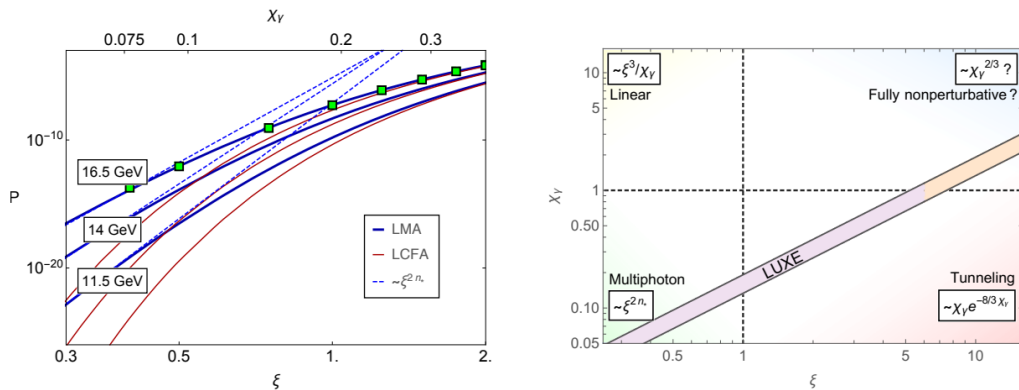

FIGURE 2.4 • **Left:** The dependency of probability for the Breit-Wheeler process on the intensity parameter ξ for a probe photon colliding at 17.2 degrees with laser pulse parameters. The blue dashed lines indicate multiphoton scaling and the plot markers are the analytical QED plane-wave results for a photon energy of 16.5GeV. **Right:** the parameter region LUXE will probe, compared to the asymptotic scaling of the Breit-Wheeler process at large and small ξ and χ parameters.

As ξ surpasses 1, the observed deviation from the perturbative multiphoton scaling regime serves as a distinct indicator of the process's non-perturbative dependence on the field strength. The LCFA provides a comparative result, but it becomes a

reliable approximation only for larger ξ. In scenarios where $\xi \gg 1$ and $\chi_\gamma \ll 1$, the Breit-Wheeler process exhibits characteristics reminiscent of tunneling. In a constant crossed field, the rate scaling for $\chi_\gamma \ll 1$ follows $\sim \chi_\gamma \exp(-8/3\chi_\gamma)$, and given that $\chi_\gamma \propto \sqrt{\alpha}$, this behavior is non-perturbative in the charge-field coupling, drawing parallels to the Schwinger effect [27]. However, a distinction arises as the Schwinger effect involves spontaneous pair-creation, while the Breit-Wheeler process is stimulated by a high-energy photon. The LUXE experiment aims to explore the parameter space between these distinct asymptotic scalings, as depicted in Fig. 2.4.

For the parameters under investigation by LUXE, the Breit-Wheeler spectrum is symmetric around $v = 0.5$ (where $v = \frac{\chi \cdot P'}{\chi \cdot K'}$ is the lightfront momentum fraction of the produced electron, where P' (K') is the emitted electron (incident photon) momentum), implying an equal distribution of the photon's lightfront momentum between the electron and positron. However, an increase in the intensity parameter broadens the spectrum, leading to a broader lightfront momentum distribution for the produced particles. The accuracy of LMA is better at small $\xi \sim O(1)$ values

To directly observe the Breit-Wheeler edges at LUXE, it would be essential to produce pairs for $\xi \lesssim 1$ while maintaining a reasonably large χ_γ. This could be achieved, for instance, through high-order harmonic generation [28–30]. Assuming a collision involving a 9 GeV gamma-ray photon, the 19th laser harmonic would be necessary to surpass the linear pair production threshold. It's worth noting that the high-harmonic light is expected to have $\xi \ll 1$. However, in this regime, as it probes the linear domain, the pair production cross section remains independent of ξ.

LUXE plans to measure the Breit-Wheeler process in two distinct configurations. The first approach involves colliding the electron beam with a solid target to produce high-energy bremsstrahlung photons. These photons will then interact with the primary laser pulse, decaying into pairs. An alternative approach involves colliding the electron beam with a weaker laser to produce a narrow bandwidth of high-energy photons through ICS [31]. These photons will subsequently interact with the primary laser pulse, decaying into pairs.

Trident Process

Trident Process

The LUXE experiment will also delve into the study of non-linear trident pair production [32–34]. This process pertains to the generation of an electron-positron pair from an electron (or positron) within the laser field. This encompasses both the inset diagram and an exchange diagram, where the outgoing electrons are inter-changed, accompanied by a relative negative sign. While there isn't a universally accepted method to separate this process into distinct components, especially for a short pulse where $\xi \approx \eta \approx 1$, a useful separation based on the pulse duration Φ is considered for longer pulses, such as those at LUXE.

The total probability can be divided into two parts: $P_t^{(2)}$, which scales with Φ^2, where Φ is the pulse duration and $P_t^{(1)}$, which scales with Φ. Applying this separation within the LCFA yields $P_t^{(2),\text{LCFA}}$, which can be factorized in terms of the rate of first-order processes of the Compton emission of a polarized photon, $R_{\gamma,j}^{\text{LCFA}}$, followed by the decay of a polarized photon via the Breit-Wheeler process, $R_{e,j}^{\text{LCFA}}$:

$$P_t^{(2),\text{LCFA}} = \sum_{j=1}^{2} \int_{-\infty}^{\infty} d\phi_1 \int_{\phi_1}^{\infty} d\phi_2 \int_0^1 ds \frac{\partial R_{\gamma,j}^{\text{LCFA}}(\phi_1, s)}{\partial s} R_{e,j}^{\text{LCFA}}(\phi_2, s) \qquad 2.3$$

Here, the summation is over the two transverse polarization states of the intermediate photons. Due to this factorization, $P_t^{(2)}$ is often termed as the "two-step" or "avalanche" or "incoherent" process, while $P_t^{(1)}$ is known as the "one-step" or "coherent" process. The leading-order behavior for $\xi \ll 1$ of each term is $P_t^{(2)} \sim \xi^4$ and $P_t^{(1)} \sim \xi^2$. Although the one-step term has the potential to dominate the probability, a sufficiently long pulse duration can allow the two-step term to offset this.

Based on this analysis, the LMA rates for the first-order processes of non-linear Compton scattering and Breit-Wheeler pair creation will be employed to approximate higher-order processes, such as trident and multiple Compton emission. Therefore, for the parameters that LUXE will use to generate pairs via the non-linear trident process, it is a good approximation to consider just the "two-step" process of non-linear Compton scattering followed by non-linear Breit-Wheeler pair-creation.

2.2.2 Kinematics in Plane-Wave Background

Processes in a plane-wave setting adhere to a unique kinematic structure. Unlike the vacuum, which maintains invariance under time and space translations, a plane-wave background introduces a preferential direction via the background wavevector. Consequently, only three energy-momentum components are conserved. This leads to the expression of SFQED process probabilities as integrals over lightfront momentum spectra.

2.2.3 Approximations in Numerical Simulations

A common approximation in SFQED phenomena simulations with intense laser pulses is the "Locally Constant Field Approximation" (LCFA) [35]. This method involves using the probability of a specific first-order dressed process in a purely constant crossed field to derive an instantaneous "probability rate", which is then integrated over an arbitrary pulse shape. For the LCFA to be accurate for LUXE's considered particle energies, it's essential for $\xi \gg 1$. Given that SFQED phenomena will be probed for a range of intensity parameters in LUXE's phase-0, the LCFA may not always provide accurate predictions. Moreover, capturing the harmonic structure in particle spectra, which emerges due to interference between emissions across the laser pulse, is beyond the LCFA's capabilities. Instead, the "Locally Monochromatic Approximation" (LMA) will be utilized, addressing the laser carrier frequency's fast timescale precisely while approximating the slower pulse envelope timescale. It is worth noting that the two approaches are complementary, the LMA is suitable for multi-cycle laser pulses, especially when minimal plasma is produced during interactions [1].

2.2.4 Probing Physics Beyond the Standard Model at LUXE

Substantial experimental evidence suggests the presence of new physics beyond the established Standard Model [36, 37]. One plausible explanation for these experimental observations entails the emergence of new, light degrees of freedom, exhibiting weak coupling to the Standard Model and potentially extended lifetimes. Axion-like particles (ALPs), being generalizations of the conjectured axion addressing the strong-CP problem [38, 39], can establish a coupling with two photons, thereby generating a discernible signal within the LUXE experiment framework. A 'secondary production' mechanism is envisaged for utilization, which encompasses the high energy ICS beam with a beam dump, followed by their downstream propagation towards a beam dump. Within this setup, ALPs may be generated (through the Primakoff effect) and subsequently decay beyond the dump into two photons. A

dedicated detector is then deployed to capture the photons, filter out backgrounds originating from, for instance, neutrons, and measure the energies and angular distribution of the photons. This aspect of the LUXE experiment is denoted as NPOD (New Physics search with Optical Dump). The interested reader can find more detail in Ref. [40].

NPOD aims to probe the pseudoscalar ALP couplings within the region of $10^{-5}\,\mathrm{GeV}^{-1}$ for pseudoscalar masses approximating $\sim 200\,\mathrm{MeV}$, a parameter space unprobed by ongoing experimental endeavors. This approach unveils a novel and complementary avenue compared to classic Light-Shining-Through-Walls experiments. For instance, in contrast to direct electron beam dumping, this strategy significantly mitigates the background interference.

Two primary mechanisms for new physics production are considered:

→ **Primary Production:** Here, ALPs, scalars, and mCPs (milli-charged particles) are generated at the LUXE Interaction Point (IP) through processes such as $e^- m m a_L \to e^- + \phi P$ and $e^- + n\gamma_L \to e^- + \phi_S$. The production rate is amplified due to non-perturbative interactions with the laser.

→ **Secondary Production:** This method considers LUXE as a GeV photon source. The emitted Compton photons in the e-laser mode scatter on a nuclear target, leading to the production of ALPs or scalars through the Primakoff process.

The maximum mass accessible in primary production is constrained by a center-of-mass energy on the order of MeV. However, secondary production can probe masses up to a few hundred MeV. Our focus is on new particles with lifetimes greater than approximately 1 ns. The detector is placed away from the production point, resembling a beam-dump setup. Fig. 2.5 shows a schematic design of the proposed setup.
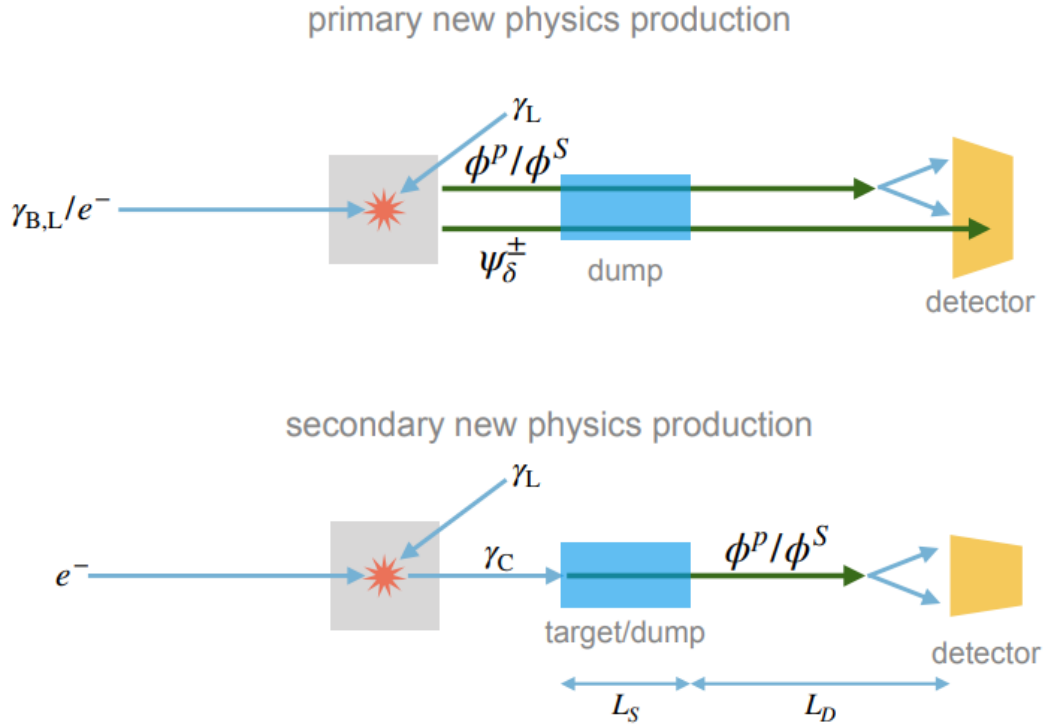
FIGURE 2.5 • A schematic design of the LUXE new physics (NP) search setup. **Top:** Primary production, where the NP is produced at the interaction point (IP). **Bottom:** Secondary production, where the high-rate Compton photons from LUXE collide with a target/dump of size L_S, resulting in the production of ALPs/scalars (represented as ϕ_P/ϕ_S in the figure). The detector is positioned at a distance L_D from the target.

For now, the attention of LUXE is on the secondary production of ALPs, reserving primary production for subsequent studies. The findings for ALPs can also be extended to scalars. The sensitivity to the photon-ALP coupling in secondary production is measured using a specific setup. The Compton photons from primary e-laser collisions interact with a dump, blocking all Compton photons. However, ALPs can be produced and decay to two photons after traveling a certain distance. A detector is positioned to capture these decay photons. This configuration is accomplished by probing ALPs with masses ranging from MeV to GeV [41].

2.3 LUXE experimental setup

A thorough characterization of the interactions that will take place in LUXE requires the measurement of the cross-section. Hence, we need to identify the particles, their energies and the angular distribution. The focal particles encompass electrons, photons, and positrons, with their fluxes. A comprehensive simulation of the

experimental domain was executed using Geant4. A more exhaustive explanation on the simulation and the results is detailed in Chapter 4 [1]. Fig. 2.6 illustrates a sketch of the experimental layout for both e-laser and γ-laser modes.
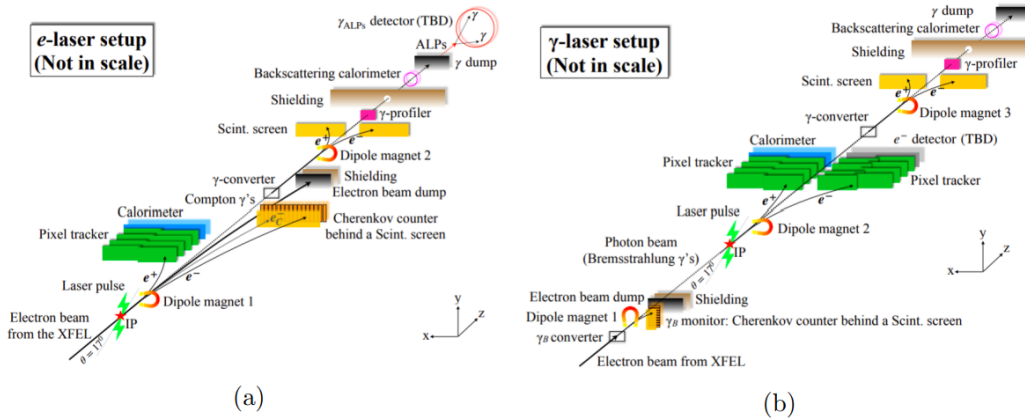

(a)   (b)

FIGURE 2.6 • Schematic layouts for the e-laser and γ-laser setup. Shown are the magnets, detectors, and main shielding and absorbing elements.

LUXE is partitioned into three distinct areas:

→ **Target area:** this area is only relevant for the ⬚-laser mode. A target chamber is installed for the purpose of converting the electron beam to a photon beam either via bremsstrahlung on a tungsten target or via inverse Compton scattering on a low intensity laser beam. Behind the target chamber there is a dipole magnet to separate electrons, photons and positrons. A scintillation screen and camera and a Cherenkov detector is installed to measure the electron flux which can be used to reconstruct the energy spectrum and measure the flux of electrons after the bremsstrahlung process. In the e-laser mode the magnet is turned off and the electrons proceed to the IP.

→ **IP Area:** at the IP, electrons, positrons and photons are expected to be produced. Behind the IP there is a dipole magnet to separate these three particles physically in the horizontal plane. Behind the magnet on the left-hand side ($x > 0$, the "positron side"), for both the e-laser and ⬚-laser setup there is a system to measure the number of positrons and their energy spectrum. It consists of a tracker [42] and a calorimeter [43]. On the right-hand side ($x < 0$, the "electron side"), in the e-laser case there is a scintillator screen with a camera [44] and a Cherenkov detector [45]. The positron rates vary between 10^4 and 10^4 per bunch crossing, and thus the technology chosen must be able to achieve an excellent background rejection (ideally $< 10^3$ per bunch crossing) to facilitate measurements at very low multiplicities, and achieve a good linearity at high multiplicities. A tracker followed by a calorimeter was chosen as these technologies are adequate for

such particle multiplicities and are very effective at reducing backgrounds from stray secondary and tertiary particles. On the electron side the particle flux is much higher for the e-laser setup and can reach values as high as 109 per bunch crossing. Therefore the technologies used here are designed to be adequate for such high fluxes. It is important that the position resolution in these detectors is high so that the energy resolution is better than 2% in order to be able to resolve the Compton edges, see Ref. [45]. The technologies chosen are Cherenkov detectors and scintillation screens. In the γ-laser case, we expect e^+e pairs to be produced with fluxes between 10^4 and ~ 10 $e^{\pm}$ per 282 BX. Thus, here a tracker and a calorimeter is used on both the positron and the electron side. Due to the low multiplicity of electrons and positrons it is possible to combine the electron and positron and thus reconstruct the energy of the initial photon event by event.

→ **Photon Area:** any photons that are produced at the IP in the e-laser mode (the Compton photons) or that fly through the IP area undisturbed in the γ-laser mode end up in the photon detection system which is designed to measure the photon flux, angular and energy spectrum. The energy spectrum is determined using a Gamma Spectrometer [46] consisting of a small tungsten target which converts photons to e^+e pairs, a dipole magnet that separates them, and two scintillation screens (with cameras) that measure the electron and positron energy spectra. It is followed by a Gamma Profiler [47], made up of two sapphire strip detectors which are designed to measure the size of the photon beam in the horizontal and transverse direction. For a linearly polarised beam the photon spot size in the two planes can be used to get an independent measurement of ξ. The sapphire detector granularity is chosen such that this can be obtained for each shot with a precision of 5%. Finally there is a Gamma Flux Monitor [48], which consists of lead-glass calorimeter blocks that were originally designed for the HERA-b experiment but were never used there. It will measure the overall photon flux and also serve as a type of luminosity monitor as the photon flux is a very good measure of the overlap between the electron beam and the laser for the e-laser setup. The Gamma Profiler and the Gamma Spectrometer are also sensitive to the photon flux.

Three beam dumps are required are necessary for terminating the electron or photon beams. They are designed to reduce back-scattering in the IP and photon area sections where signal particle rates are low. Furthermore shielding components are placed to further reduce the background radiation based on a full simulation of the experimental area with Geant4 [49, 50].

LUXE embodies a modular architecture, comprising a series of independent segments which are readily accessible whenever access to the tunnel is permitted. This modular design enables a staged installation, dependent on the readiness

and/or necessity of a given detector piece. It is envisaged that the installation of all components will be prepared and tested on the surface well in advance to minimize the time required for in-tunnel installation.

Given the potential uncertainties on the time scales on which all the detectors can be ready, it is prudent to envisage a minimal version of the LUXE experiment that could be prepared for initial data acquisition. A conceptual sketch of such a minimal version is showcased in Fig. 2.7. This minimal version could be deployed for a preliminary measurement of the Compton process via the measurement of the electron spectrum with the scintillation screen and/or Cherenkov detector. Additionally, the already existent prototype of the CALICE [51] calorimeter could be installed on the positron side and could be harnessed to measure the number of positrons within the confined energy range of about $4 - 8$ GeV. Moreover, the back-scattering calorimeter provides a measure of the photon flux. It is crucial to emphasize that such a minimal version is capable of covering merely a fraction of the LUXE physics programme, but it would already facilitate some physics measurements, even if several detectors are delayed due to, for instance, delayed delivery of components, scarce resources, or technical difficulties.

In principle, any scenario ranging from the bare minimum to the full version should be conceivable depending on the readiness of the components. For instance, if available, tracker half-layers could be installed in front of the calorimeter (see next-to-minimal version in Fig. 2.7).
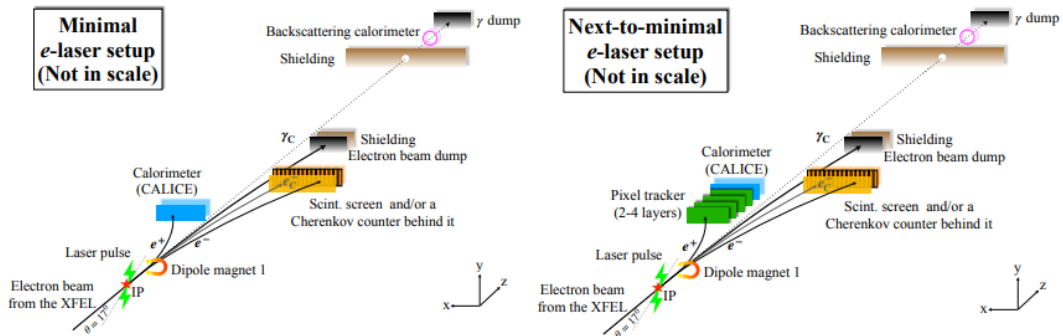

FIGURE 2.7 • Schematic layouts for a minimal (**left**) and a next-to-minimal (**right**) version of the LUXE experiment for the e-laser setup. Shown are the magnets, detectors and main shielding and absorbing elements.

2.3.1 Photon Detection System

In the scenario of e-laser interactions, insights are encapsulated in the energy spectrum and the angular distribution of photons downstream from the interaction area. The spectrum of the photon beam generated through the Compton

process, $e^- + n\gamma_L \rightarrow e^- + \gamma$, in the laser field, allows to identify and study several distinctive features particularly the Compton edges in the energy spectrum. A precise articulation of the angular distribution of the photons birthed in the interaction will also enable an independent determination of the laser dimensionless intensity ξ. Assuming a linearly polarized laser pulse, which is the desired operation mode, and a negligible divergence of the primary electron beam, the photon beam divergence along and transversely to the laser polarization axis are approximately $\theta_\parallel = \max(\xi, 1)/\gamma$ and $\theta_\perp = 1/\gamma$, respectively [52, 53]. The ellipticity of the photon beam then directly reflects the ξ value experienced by the electron beam.

These diagnostics are important not only for the examination of non-linear Compton scattering and radiation reaction but also serve as a valuable shot-by-shot tagging mechanism to monitor the laser shots' stability and to potentially discard shots with, for example, sub-optimal electron-laser overlap or other undesired attributes. The total photon flux as a function of energy is another measurable quantity and is crucial for BSM physics programme in e-laser collisions, while in γ-laser collisions, it offers an independent measure of the flux of bremsstrahlung photons.

Three detector systems are envisioned for this purpose:

→ A Gamma Ray Spectrometer (GRS) that determines the photon energy spectrum by measuring the spectrum of secondary electrons and positrons generated during the photon beam's interaction with a solid converter.

→ A Gamma Beam Profiler (GBP) that measures the energy-integrated spatial distribution of the photons.

→ A Gamma Flux Monitor (GFM) that measures the relative flux of photons via a backscattering calorimeter.

These detector systems are planned to be situated between the termination of the vacuum pipe, post the positron and electron detection systems, and the tunnel's end. It's presumed that the vacuum pipe concludes before the photon detection system components, leading to particle scattering in the air.

Introduction to Gamma Beam Profiler (GBP)

The Gamma Beam Profiler (GBP), which will be discussed in details in Chapter 3, is devised to measure the angular distribution of the photons, with a precision corresponding to about $5\,\mu m$ in x and y at 11.5 m downstream the IP. It is envisaged to be a pair of two sapphire strip detectors with a pitch of $100\,\mu m$, staggered behind each other with a relative rotation of $90°$.

The profiler must operate reliably amidst a highly intense high-energy gamma-ray flux. The typical photon energy is in the GeV range, where electron-positron

pair production is the dominant process in the profiler.

It is necessary for such a profiler to be radiation hard at a level of several MGy per year and have the ability to reconstruct the beam profile position and width with a spatial resolution of around $5~\mu\mathrm{m}$. The GBP is the only LUXE profiler that can provide information on the spatial distribution of the produced gamma-ray photons. Therefore, it is necessary to have a very reliable detector that can provide the beam profile information to the experiment from the beginning. During the first commissioning, the optimization of the e-laser interaction is critical to understanding the quality of the interactions.

CHAPTER 3

Gamma Beam Profiler

Artificial sapphire, characterized by a wide bandgap of $9.9\,$eV, emerged as a noteworthy material in high-energy physics over the past decade, particularly as a particle detector, marking a significant milestone in this field [54]. Sapphire, distinguished by its mechanical and electrical properties, and Its capacity for mass production in industrial contexts makes it a feasible alternative. Recent advancements showcased the utility of optical grade sapphire as a detector material, even without additional purification. This development elevates sapphire's status as an advantageous choice, attributed to its cost-efficiency and radiation hardness.

Despite the relatively small signals of 22 electron-hole (eh) pairs per micron of a Minimum Ionizing Particle (MIP) track and a low charge collection efficiency (CCE) (which will be explained in detail in Chapter 4) of around 10%, sapphire detectors demonstrate a remarkable capability in handling large fluxes of particles concurrently impinging on the detector. A notable advantage is the low leakage current ($\sim pA$) at room temperature, even after high-dose irradiation, rendering these detectors almost noiseless. These attributes underscore the potential of sapphire in transcending the limitations observed in silicon and diamond sensors, traditionally used in such applications.

In this chapter, we delve into the historical evolution of sapphire and explore its fundamental attributes, laying the groundwork for a thorough discussion on the strides made in sapphire GBP technology.. Lastly, we discuss the GBP technical description, including the electronics design.

3.1 Artificial Sapphire

Artificial sapphire, a crystalline form of Al_2O_3 with the same lattice structure as diamond, is the topic of focus. While natural sapphire and ruby can be found around the globe, they are particularly abundant in Africa, Asia, Australia, North America, and Europe [55].

Over 300 years ago, sapphire was first used in industry as a durable and low-friction component in mechanical watches. With the first synthetic ruby grown in the 1880s and mass production beginning in 1900, rubies and sapphires became useful for various industrial purposes. This section will discuss the creation of artificial sapphire, different techniques for growing it, its fundamental characteristics, and its applications.

3.1.1 History of artificial sapphire

The roots of artificial sapphire synthesis trace back to 1817, when J.L. Gay-Lussac unveiled a method for obtaining pure aluminum oxide. This compound later established itself as the bedrock for sapphire production. However, the journey from discovery to functional cultivation of sapphire was not straightforward. In 1877, Edmond Fremy and his collaborator Charles Feil achieved a notable milestone by producing small ruby crystals, setting a precedent for larger-scale synthesis [56].

Building upon Fremy and Feil's foundation, Verneuil significantly advanced the field. By 1904, he had perfected the flame fusion process for ruby synthesis, a method that became seminal in sapphire production. This achievement, depicted in Fig. 3.1, was a monumental step in the artificial production of gem-quality crystals [57].

The onset of the 20th century saw Europe pioneering the Verneuil method. The adoption of this method grew exponentially, and by the 1930s, the Soviet Union's innovations had further refined it. They introduced enhancements that produced superior quality sapphire rods suitable for various applications. The mid-20th century, particularly the era following the 1960s ruby laser invention, marked the rise of the Czochralski technique. This method, showcased in Fig. 3.2, enabled the growth of significantly larger sapphire crystals [58, 59].

By 2003, the sapphire production landscape had transformed remarkably, with an impressive 250 tons produced annually. The versatility of sapphire ensured its integration into diverse sectors. From electronics to semiconductors and lasers, the material's unparalleled properties made it indispensable [60–62].

Emerging from these innovations and demand, certain countries positioned themselves as industry leaders. The U.S. and Russia, in particular, consolidated their dominance in the global sapphire market. Their contributions have greatly shaped the trajectory of sapphire synthesis and applications [63].

FIGURE 3.1 • Flame-fusion synthetic sapphire crystals, as-grown (left) and during growth (right). Courtesy of Hrand Djevahirdjian, SA [59].

FIGURE 3.2 • A Czochralski-grown synthetic ruby crystal with a fabricated piece (left) and during extraction (right). Photos by Jennifer Stone-Sundberg [59].

3.2 Research and development of GBP technology

3.2.1 Basic features of artificial sapphire and industrial applications

Sapphire, a durable and stable material, can withstand high temperatures, rapid heating and cooling, high pressure, and chemical corrosion. It has a hardness of 9 on the Mohs mineral scale, second only to diamond [56]. When free from impurities that give it color, sapphire is transparent across the visible range, as well as the UV and IR ranges, making it an exceptionally hard material [59]. Sapphire is also used as a substrate in the semiconductor industry for epitaxial silicon growing, blue light-emitting diodes production, and laser diodes [64] [65].

Additionally, sapphire's lattice structure makes it an excellent substitute for epitaxial grooving of silicon, with computer and smartphone chips often being grown on sapphire due to its thermal conductivity. Consequently, it is a novel material for use in gamma beam profiling due to its radiation-hard properties that can operate with a total intensity per bunch crossing (BX) of the gamma beam $\phi = 10^7 - 10^9$ photons/BX. Given the very high flux the material needs to withstand, sapphire detectors are proposed due to their intrinsic radiation hardness, which can reach up to $10\,\mathrm{MGy}$. These detectors maintain robust performance with minimal degradation even when exposed to high doses of radiation [54]. Notably, sapphire is an artificial wideband-gap insulator that has gained interest as an active material in radiation detectors in harsh environments [66].

3.2.2 Sapphire as a solid state detector

In order to use sapphire crystal as a solid state detector, certain conditions must be met, which are:

1 an ionizing particle must create enough charge carriers to be detected

2 the lifetime and mobility of the charge carriers should allow them to drift through a significant portion of the sensor's thickness

3 It is essential to have low leakage current to prevent noise

Additionally, when an ionizing particle passes through the crystal, it loses energy that causes lattice excitation and generates free charge carriers. The mean energy required to produce one electron-hole pair, related to the bandgap energy, is estimated to be 27 eV for sapphire crystal. This energy value varies depending on the semiconductor material and is determined either experimentally or through theoretical calculations [67] [54]. In Ref. [68], the mobility of electrons in sapphire crystals was studied at zero applied electric field and found to be high enough to generate fast signals needed in high energy physics applications.

Electron mobility within a material quantitatively describes the ease with which electrons can move through a material under the influence of an electric field. It is quantified as the ratio of the drift velocity of the charge carriers (electrons) to the applied electric field. High electron mobility is essential for the effective functioning of single-crystal sensors. This characteristic enables charge carriers to traverse the sensor material smoothly and rapidly, enhancing the sensor's responsiveness and efficiency in detecting and conveying electrical signals. A material with low levels of impurities will typically exhibit higher electron mobility. Hence, to ensure that charge carriers have a long lifespan, it is necessary to have single crystal sensors with few impurities. Sapphire is renowned for being one of the best insulators due to its wide bandgap, which causes low leakage current at room temperature and a high breakdown field. Additionally, signals from sapphire sensors exhibit similar time characteristics to those from CVD diamond sensors [69]. The mobility of charge carriers in ionic crystals like sapphire changes significantly with temperature. Electron mobility in sapphire ranges from $600 \text{ cm}^2/(\text{V} \cdot \text{s})$ at 20 C to $30000 \text{ cm}^2/(\text{V} \cdot \text{s})$ at 40 K [68].

Material properties	sapphire	diamond	silicon
density, g/cm^3	3.98	3.52	2.33
bandgap, eV	9.9	5.47	1.12
energy to create an eh pair, eV	27	13	3.6
dielectric constant	9.3 - 11.5	5.7	11.7
dielectric strength, V/cm	4×10^5	10^6	3×10^5
resistivity, $\text{Ohm} \cdot \text{cm}$ at $20\,^\circ\text{C}$	10^{16}	10^{16}	10^5
electron mobility, $\text{cm}^2/(\text{V} \cdot \text{s})$ at $20\,^\circ\text{C}$	600	1800	1500
MIP eh created, eh/cm	22	36	73

TABLE 3.1 • Relevant material properties of sapphire, diamond and silicon [70, 71].

At cryogenic temperatures, sapphire sensors are predicted to have full CCE and incredibly rapid signals. Tab. 3.1 lists essential properties of sapphires for comparison with diamonds. Most notably, sapphire's larger bandgap requires twice

as much energy to create an electron-hole pair compared to diamond, resulting in higher energy loss when a charged particle moves through it. Hence, the amount of energy generated per unit length in sapphire is approximately 60% less than that in diamond.

3.2.3 R&D of sapphire sensors

Recently, the field of particle physics has witnessed significant progress, particularly in the development of highly radiation-resistant sensors designed for monitoring close to the beam pipe within particle physics experiments. These sensors are instrumental as beam halo and beam loss monitors at facilities like LHC, FLASH, and XFEL. Prior to the introduction of the GBP in LUXE, artificial diamond detectors were the standard choice in radiation-intense environments due to their effectiveness in such conditions. However, despite their widespread use, these detectors have limitations, particularly in terms of cost and scalability. This has prompted the investigation into single crystal sapphire sensors as a potential solution.

Investigations conducted on mono-crystalline sapphire sensors unveiled promising results concerning radiation hardness. For instance, sapphire sensors exhibited a smooth decline in CCE with the increase in absorbed dose, retaining around 30% of the signal of non-irradiated sensors post a dose of $12\,\mathrm{MGy}$. Additionally, sapphire sensors were installed and successfully commissioned as beam halo monitors at the FLASH facility, alongside pCVD diamond sensors, showcasing their practical applicability and operational reliability [72].

A notable study [54] showcased a multichannel, direction-sensitive sapphire detector stack, composed of eight sapphire plates metallized on both sides to form a stack. The study revealed a CCE reaching about 10% at 950 V, with a signal size of about 22000 electrons obtained from electrons traversing the stack at this voltage.

Furthermore, the successful commissioning of the Beam Halo Monitor for Free-electron Laser in Hamburg (FLASH), which utilized both pCVD diamond and monocrystalline artificial sapphire sensors, further emphasized the potential of sapphire sensors in beam monitoring applications [72]. The experience garnered from the FLASH facility has not only demonstrated the operational feasibility of sapphire sensors but also sparked ideas regarding the design and operational aspects for similar systems in FLASH II and the European XFEL.

In the context of LUXE, the development of GBP aims to leverage the promising attributes of sapphire sensors. The GBP endeavors to provide a reliable, cost-

effective, and radiation-hard solution for monitoring applications. The research, development, and the subsequent application of sapphire sensor technology in the GBP are envisaged to significantly contribute to the advancement of detector technologies in high radiation environments, particularly in the realm of collider and particle physics [73].

3.3 Technical description

This section provides an overview of the electronics design for GBP, focusing on the specific requirements and components involved. It outlines the main characteristics for GBP electronics such as its readout system. This system comprises the A5202 front-end card, capable of reading 64 channels, and the DT5215 data concentrator, which manages multiple front-end units.

3.3.1 Electronics

The main characteristics to take into account the design of the detector electronics are the following:

→ the central strips will deliver plenty of signals, of the order of tens of pC;

→ a dynamic range of 12-13 bits will be more than sufficient in order to reconstruct well the tails of the gamma beam profile distribution and to measure the beam intensity with a precision at percent level;

→ the acquisition rate will not be higher than 10 Hz.

Given the signal abundance and the low acquisition rate, the design of the electronics is considered quite straightforward. The CAEN company has developed the high-scalable system FERS-5200 [74] which matches all these requirements and this is proposed as the baseline readout system for the GBP. The FERS-5200 system consists of:

→ an A5202 front-end card, reading 64 channels at time. Three front-end cards will be therefore needed to read out one plane of 192 strips;

→ a DT5215 FERS data Concentrator, which can connect and manage up to 16 A5202 units in daisy chain for each of its 8 TDlinks inputs.

The FERS-5200 system has been designed for the readout of large detector arrays, such as SiPMS, multianode PMTs, Silicon strips detectors and many others, and it can be adopted also for the GBP sapphire strips detector readout. A description of each of these modules is reported in the following [75].

The A5202 front-end card

The front-end card is based on the Citiroc 1A ASIC [76] whose block scheme is reported in Fig. 3.3. One ASIC is able to read 32 channels. Citiroc 1A is compatible with positive-charge signals. Two measurement lines with different gain (1 to 10 ratio) are working in parallel in order to maximize the dynamic range of Citiroc 1A. For each channel, two parallel AC coupled voltage preamplifiers are embedded to ensure a dynamic range from about 10 fC to about 100 pC (the full range could actually be 400 pC), well suited to accommodate the different amount of collected charge from different strips. Each preamplifier is followed by a variable shaper with an adjustable time constant (from 12.5 ns to 87.5 ns with a 12.5 ns pitch) to filter the signal bandwidth and optimize the signal-to-noise ratio (S/N). The signal from the two shapers can be sampled using either a sample & hold controlled by an external signal (all the 32 channels are held at the same time) or by a peak-detector disabled by an external signal.
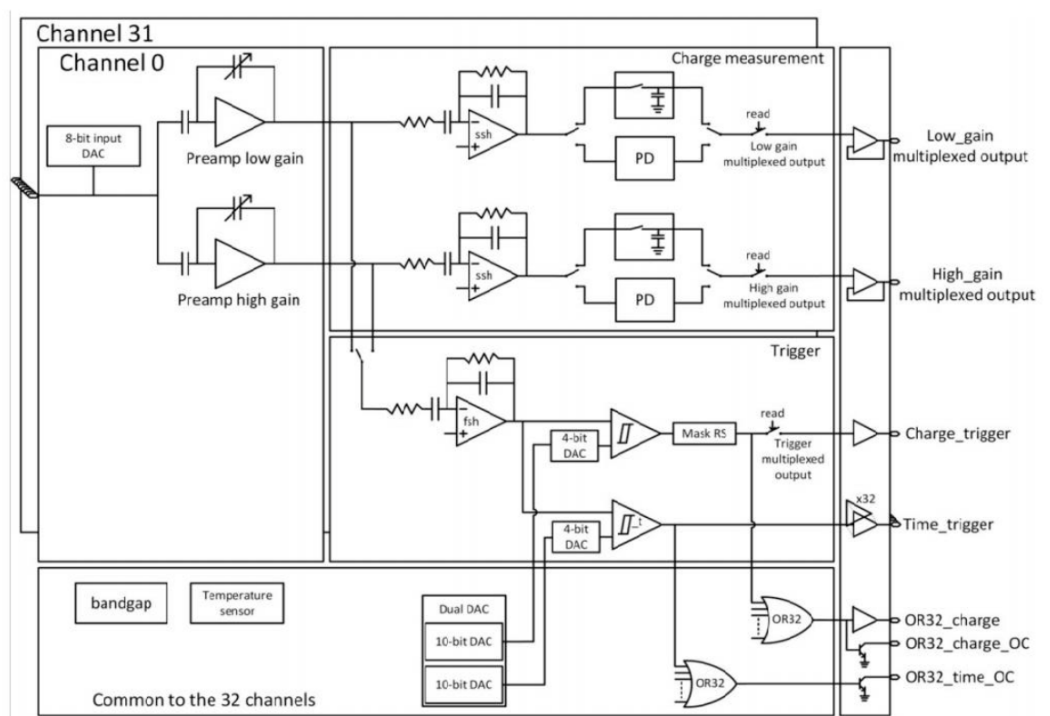
FIGURE 3.3 • General ASIC block scheme

The GBP will use the former of these two features since the charge integration will allow to achieve a better S/N. The stored charge information is read-out in serial using two analogue multiplexed outputs, one for low gain and one for high gain. The multiplexed outputs are controlled by a read shift-register. Both information of low gain and high gain of the same channel are present at the same time. Along the two charge measurement information, a hit-register provides a trigger status information.

This trigger status information will be used for debugging purposes in the lab or in the test beam, but will not be relevant for the LUXE data acquisition mode which is planned to record all the BX data.

Each channel of Citiroc 1A embeds two channel-by-channel independent programmable variable-gain preamplifiers ensuring a wide coverage of the dynamic range depending on the application (see Fig. 3.4). Both low gain and high gain preamplifier can be tuned on 6 bits (Cf can be tuned from 0 to 1575fF with a step of 25fF). The voltage gain is given by Cin/Cf, Cin=15pF for high gain and 1.5pF for low gain. Any channel preamplifier can be shut down by slow control bit to disconnect any noisy channel from the measurement chain. A calibration input is included in each channel and can be enabled individually by slow control parameters. In order to have a good precision, only one calibration input should be allowed at the same time. The injection calibration capacitance value is about 3pF. Two CRRC slow shapers are connected on the two preamplifiers outputs for each channel. The peaking time of each slow shaper can be tuned from 12.5 ns to 87.5 ns with a 12.5ns pitch. The peaking time is set commonly for all the 32 channels, however it can be different between low gain shaper and high gain shaper. A 15 ns peaking-time fast shaper can either be connected to the high gain preamplifier or to the low gain. That connection is set by slow control. The fast shaper peaking time and gain are not programmable. The fast shaper is used to provide trigger output which is of limited interest for the LUXE running mode. Each A5202 front-end card will contain two Citiroc 1A asics, so allowing the readout of 64 channels. The board logic will allow to configure the readout channels, to transmit the readout data to the DT215 data concentrator, and to make a 13 bit conversion for each analog level from the track and hold capacitors.
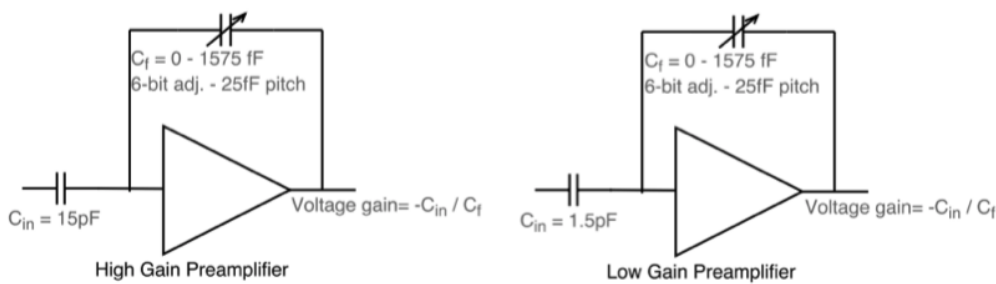
FIGURE 3.4 • High gain and low gain voltage sensitive preamplifier

The DT5215 data concentrator

One DT5215 (FERS Data Concentrator) can manage up to 8 TDlinks (optical links, 4.25 Gbps each), each connected up to 16 FERS units in daisy chain: in the case of the A5202 FERS unit, it makes 8192 readout channels. The Data Concentrator is connected to a Host computer through a 1/10 Gb Ethernet or USB 3.0. A Linux-based Single Board Computer is embedded in the Concentrator board. It manages the data readout from the network of FERS units and the event data building according to the time stamp and/or trigger ID of the event fragments acquired by each unit. Sorted and merged data packets are then stored to the local memory and finally sent to the host computers through a fast 10 GbE or USB 3.0 link. The decision about which of the two options to adopt, has still to be taken. Custom algorithms for data processing and reduction will be developed and uploaded into the embedded CPU to fully integrate the system in the LUXE data acquisition system based on EUDET.

Readout system description

Each sapphire strip detector will need three A5202 front-end cards to be read out, for a total of 192 readout channels per detector. The three cards will be plugged in a patch panel collecting the signals from the one detector (fed into kapton flat cables) and distributing them to the A5202 front-end card. The patch panel will be mounted in the platform supporting the detector in proximity of the two detectors themselves. In this way, the front-end will be placed very close to the detector, in a configuration which should optimize the obtainable S/N. One patch will be needed to read out a station of two X-Y strips detectors, so accommodating the insertion of 3+3 front-end cards. The three cards reading out one strip detector will be daisy chained together via short optical fibres, and the overall output fed in a "long" (about 20 m) fibre connecting via a fast TDlink (4.25 Gb/s)) the front-end to one input of the DT5215 data concentrator box placed in the experiment counting room. The system is modular, and a second station with another pair of X-Y sapphire strips detector can be easily added in the future. Use of common flat cables and adapters to connect the detectors to FERS is shown in Fig. 3.5.
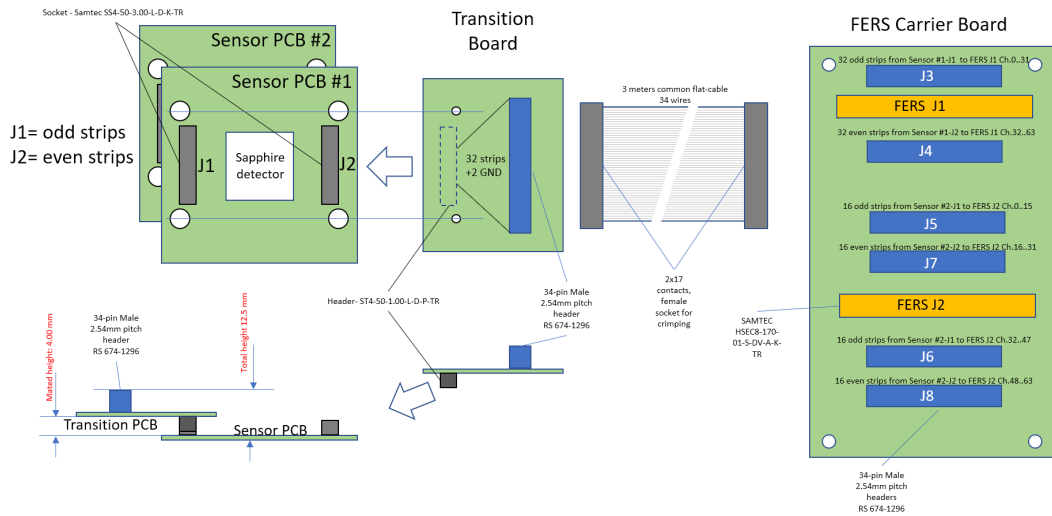
FIGURE 3.5 • The connections of flat cables and adapters to FERS

The way the detector will be connected to the HV system and to the front-end card is sketched in Fig. 3.6. Due to the very different mobility of electrons and holes in sapphire, the proposed connection will allow to have positive input signals (as required by the A5202) and full collection of charge also for ionization created by gammas which convert to electrons in proximity of the detector strip.
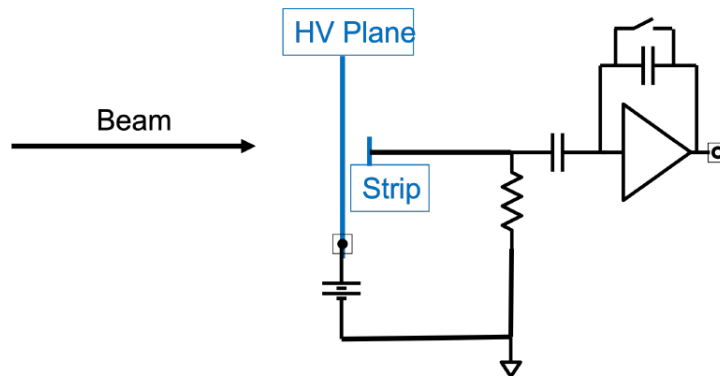

FIGURE 3.6 • Connection of the detector to the HV

High and Low voltage systems

For powering the detector and the associated electronics the SY5527LC modular system developed by CAEN is proposed [77]. The system is based on a main crate (SY5527LC) which will host one LV card (A2519CA) to power the electronics and one HV card (A1561H) to power the detectors. The crate, with its HV and

LV cards will be placed in the experiment counting room at about 20m distance from the detector. One HV card and two LV cards will be sufficient to power two detector stations (4 sapphire strip planes). The system will be fully configurable and controlled by remote. The HV card (A1561H) will provide up to 1 kV/20 μA per channel with the possibility to read out the current with default precision of 50 pA. The CAEN company could improve the latter parameter if necessary. The board is designed in order to provide the HV with a common floating return which is a very important option to possibly decouple the grounding of the detector from the grounding of the HV.

Monte Carlo GBP simulation

Monte Carlo (MC) simulations are essential for analyzing detector responses in high-energy physics. Hence, a standalone MC simulation is set up in order to investigate and characterize the detector response in detail. This simulation is an important tool to optimize the digitization of GBP in the framework of LUXE. Notably, the full LUXE experiment simulates the spatial distribution of the Compton-scattered photons hitting the detector in FLUKA [43]. However, the standalone MC simulation considers only the particles that enter the GBP volume, which are the particles that induce signals to model the detector response. Moreover, due to the demanding requirements of the full LUXE simulation in terms of computational resources and time needed, we consider the standalone MC simulation.

The main purpose of the standalone MC simulation is to generate a gaussian beam by accounting for the proper properties and number of the electrons in the beam, then model the detector response and finally optimize the digitization parameters. The experimental layout is implemented in detail in GEANT4 [49, 50].

The primary objectives of the MC simulation in this study are:

→ (a) Model the detector response.

→ (b) Optimize digitization parameters.

→ (c) Compare simulation and experimental outcomes.

4.1 Geant4 simulation

This section provides an overview of the simulation techniques and geometry. A simulation of particles (electrons or photons) considering two sapphire microstrip detectors of LUXE is performed to estimate the number of particles from SFQED interactions and reconstruct the energy profile from the beam. The simulation is also used to optimize the front-end electronics parameters.

4.1.1 Geometry of the simulation

The Geant4 version is 11.00, with the FTFP-BERT physics list, is used to implement the geometry model for GBP. In the coordinate framework of the geometry, a right-handed system is used. Within this system, the z-axis is aligned with the nominal direction of the beam. The y-axis is designated as the vertical axis, and the x-axis, representing the transverse direction, is positively oriented to the right of the beamline when viewed from the perspective of the beam. Fig. 4.1 displays the present detector design that was implemented: there are two sapphire microstrip sensors, separated from each other by $2\,\mathrm{cm}$ and placed $10\,\mathrm{cm}$ downstream the beam pipe window, which is implemented by $5\,\mathrm{cm} \times 5\,\mathrm{cm} \times 200\,\mu\mathrm{m}$ kapton. Noteworthy, the simulation is filled with air. The simulation starts with initial particles (either electrons or photons) from the gaussian beam generator. A detailed amount of information - i.e energy deposited from each particle- is recorded inside the volumes of the upstream/downstream detector, giving the possibility to study the energy profiles after the beam particles have interacted with the sapphire.
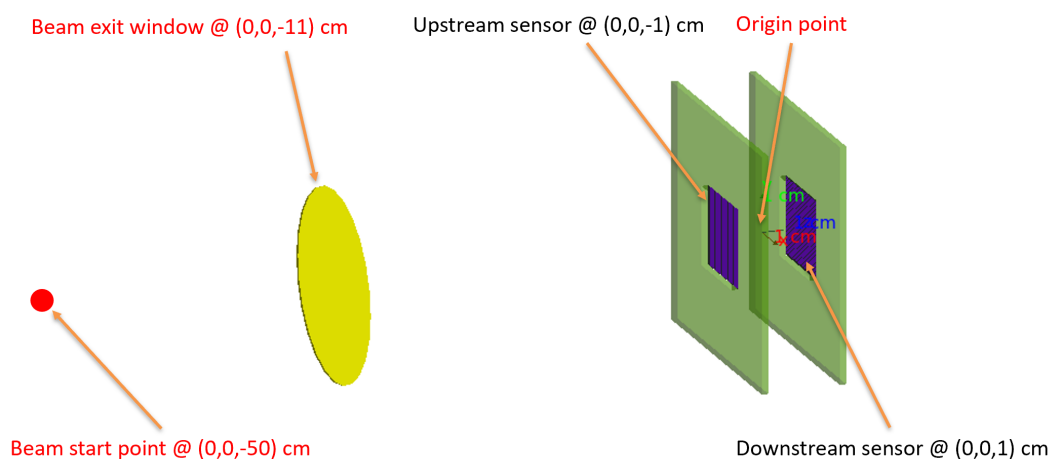
FIGURE 4.1 • The layout of the standalone MC simulation, which shows the sapphire microstrip sensors, beam start point and exit window.

4.1.2 Gaussian beam generator

The first step in starting the simulation involves implementing a gaussian distributed beam generator that allows to control the relevant parameters of the gaussian generator. The particle gun type, energy and momentum are controlled using user interface (UI) macro commands. The main particle types that were simulated are electron (e^-) and photons (γ) with energy of 1 GeV and momentum vector of $(0, 0, 1)$ GeV. The specifics about the values used in the simulation are explained in Section 4.4.

In order to have full control of the beam characteristics, new functions are defined in the detector messenger class to set the mean and standard deviation of the gaussian distributed beam. These parameters are initial position vector (x_0, y_0, z_0) and beam width for three axes $(\sigma_x, \sigma_y, \sigma_z)$. Additionally, it was necessary to develop new function to set a three-vector for the direction of the momentum of the initial particles (u_x, u_y, u_z).

4.1.3 Upstream and downstream sensors

This crucial step encompasses the construction of the sensors, in which they are constructed from a wafer with the following size: $x = y = 20$ mm and thickness of 100 μm. On the top and bottom of the sapphire wafer, there are metallization volumes with an array of 192 strips with a width of 80 μm and a spacing among each strip of 20 μm which make a strip pitch of 100 μm. The metalization volumes are built with dimensions of $x = 20$ mm, $y = 80$ mm and a thickness of 100 nm.

The next figures display the origin axes with the PCB support base and the sensor in the middle is made of sapphire for the upstream Fig. 4.2a and downstream Fig. 4.2b sensors. It is important to note that, for the purposes of the simulation, only materials on and around the beamline are relevant and depicted.

(A) The upstream microstrip sensor with horizontal placed strips.

(B) The downstream microstrip sensor with vertical placed strips.

FIGURE 4.2 • The upstream/downstream sapphire microstrip sensors (colored in purple) with 192 strips placed horizontally and vertically showed in black lines respectively, the green area around the sensors is the PCB base and origin axes in the middle of the sensors.

In the standalone MC simulation, when a particle enters the upstream/downstream sensor, it loses energy as it interacts with the Sapphire material. The energy deposited by the particle is recorded as a hit by the sensor. The hit contains information about the position, energy, and time of the interaction. This information is relevant to use for the digitization module.

4.2 Digitization module

Digitization is a complex process that involves the generation of charge propagation and accounts for all the effects that should be considered in a proper simulation. For simulating the electric signal generation and its subsequent digitization, a **simple** digitizer has been developed using Python and ROOT. The simple digitizer is a script that performs digitization after the Geant4 simulation, starting from the profile of energy deposition to charge collection within the sapphire sensors. It encompasses an algorithm designed to simulate the strip cross-talk effect and incorporates the application of front-end electronics. The latter are parameters that construct a phase space to study the effects of each of them.

The steps of digitization are visualized in Fig. 4.3.

Digitization Pipeline

readEdepFromROOT

fromEnergyToChargeDeposited

calculateProfileStatErrs

makeProjChgProfs

simulateCrosstalk

applyNoise

applyAmplification — Front-end electronics

applyADC

getDigitizedProfiles
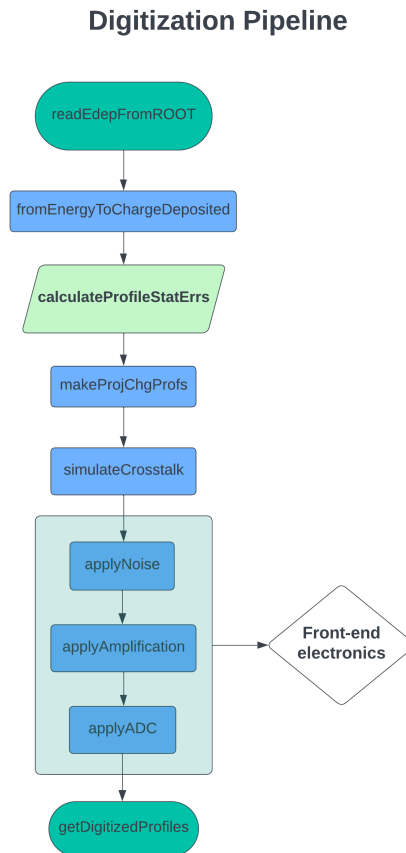
FIGURE 4.3 • A flow chart showing the digitization steps with the functions names.

Hence, the digitizer pipeline is developed to:

1 Read and bunch split energy maps from MC simulation.

2 Define the charge deposition function.

3 Define the charge collection efficiency function.

4 Define strip cross-talk algorithm.

5 Define front-end electronics parameters and functions.

6 Reconstruct the gamma beam profile.

7 Optimize digitization parameters that impact the resolution of the detector.

4.2.1 Energy maps reading and bunch splitting

The function `readEdepFromROOT` processes ROOT files provided by the standalone MC simulation. The function operates on the principle of dispatching based on the number of particles per bunch. The ROOT file input is expected to contain $N \times M$ physical bunch simulations, where N is the number of bunches and M is the number of particles per bunch. The function executes a series of operations:

$\rightarrow$ First, it attempts to load pre-calculated data from a NumPy binary file, significantly reducing computation time if the data already exists.

$\rightarrow$ If no pre-existing data is found, the function proceeds to read the ROOT file.

$\rightarrow$ The number of bunches is then determined by retrieving the number of entries in the file.

$\rightarrow$ For each bunch, the profile of energy deposition as a function of the strip number in the upstream and downstream sensors is calculated.

The core of the function's logic lies in the projection of the energy deposition onto TGraphs that represent the sensors. The energy deposition maps are then filled with the corresponding data for each bunch, effectively splitting the data according to the number of particles in each bunch.

4.2.2 Charge deposition function

This function imports a profile of energy deposited (in keV). The conversion from energy deposited to deposited charge process happens based on Shockley–Ramo theorem (for more details, see Ref. [78]) in radiation sensors. However, we simplify this process by using the mean pair creation energy as a first approximation.

Notably, we neglect the complicated profile of charge depositing along the thickness-direction of the sensor and assume that the total energy deposition is proportional to the charge collection efficiency (which is explained in detail in the next subsection).

Given an energy deposition profile, $E_{\mathrm{dep}}(x)$, summing it over 100 μm of the strip N and attaching to the point at strip = N in the TGraph, the corresponding charge deposition, $Q_{\mathrm{dep}}(x)$, can be expressed as:

$$Q_{\mathrm{dep}}(x) = E_{\mathrm{dep}}(x) \times \frac{e}{E_{eh}} \qquad 4.1$$

where e represents the elementary charge and E_{eh} is the average energy needed to generate an electron-hole pair in sapphire.

4.2.3 Charge Collection Efficiency (CCE)

In a sapphire sensor, the charge created by an incident particle is collected by the electrodes of the sensor. The CCE is important when considering the scenario where the charge is uniformly distributed across the sensor thickness, as is the case when an electron traverses the sensor.

The CCE of uniform charge deposited is derived from the charge induced by a moving charge and integrating the Hecht equation over a uniform charge distribution, we obtain [79]:

$$CCE_{uniform} = k \left(1 - k \left(1 - e^{-\frac{1}{k}}\right)\right), \quad \text{with } k = \frac{\mu \times \tau \times V}{d^2} \qquad 4.2$$

where:

→ μ represents the electron mobility.

→ τ denotes the lifetime of the charge carrier, that is the time the carriers propagate before recombining.

→ V is the biasing voltage applied across the sensor.

→ d indicates the sensor's thickness.

This equation takes into account the key physical attributes of the sensor, such as electron mobility, lifetime, applied voltage, and thickness, and how these factors influence the CCE.

It is important to note that the formula simplifies under the condition $k \ll 1$. In this scenario, the CCE can be approximated as:

$$CCE_{uniform} \approx k \qquad 4.3$$

In materials with a wide bandgap, like sapphire, the mobility of holes is significantly lower than that of electrons. Hence, their contribution to the CCE is deemed negligible, allowing the model to focus exclusively on electron dynamics [80] [81].

Within the digitization pipeline, the CCE is a modifiable parameter that is tuned in accordance to the operational voltage, which spans from 100 V to 1000 V. This adaptability offers flexibility for choosing the dynamic range of the FERS to be used for the sensor.

Statistical error computation

The error associated with the energy deposition is computed by evaluating the standard deviation of the charge accumulated on each strip over the entire simulated dataset. The purpose is to calculate the statistical uncertainty associated with the charge deposited on each strip for all the bunches in a given run. This process involves a transformation from energy deposition data to charge deposition, which is then used to compute the standard deviation across the bunches, thereby yielding the uncertainty for each strip.

The statistical error function computes the standard deviation $\sigma_{d,s}$ of the charge deposited on each strip s for a given detector d across all bunches:

$$\sigma_{d,s} = \sqrt{\frac{1}{N-1}\sum_{b=1}^{N}\left(Q_{d,s}^{b} - \overline{Q_{d,s}}\right)^2} \qquad 4.4$$

where N is the total number of bunches, $Q_{d,s}^{b}$ is the charge deposited on strip s of detector d for bunch b, and $\overline{Q_{d,s}}$ is the mean charge deposited on strip s.

The standard error for each strip is then normalized by the square root of the number of bunches:

$$\epsilon_{d,s} = \frac{\sigma_{d,s}}{\sqrt{N}} \qquad 4.5$$

This normalization accounts for the sample size of the bunches, yielding an uncertainty measure scaled appropriately for the number of observations.

The function returns an array, ϵ, containing the uncertainties for each strip across detectors. This array is fundamental to the subsequent analysis of uncertainty; attaching the errors to the charge deposited on each strip for all the bunches in a given run will result in propagating the errors through the entire pipeline. In return, these attached errors will be used for the fits with the gaussian model.

4.2.4 Strip cross-talk algorithm

Cross-talk is a phenomenon that can significantly impact the performance of the sapphire sensors. As a first approximation of cross talk, it is associated with the process of charge sharing, which occurs when a charge spreads over multiple strips. This spreading leads to a situation where the charge is not confined to a single strip where the charge collection initially occurred but is instead shared among neighboring strips.

In the simple digitizer module, the `simulateCrosstalk` algorithm redistributes charge among neighboring strips in the sensor. The input to this function is a ROOT `TGraphErrors` object, containing the charge profile across strips. For a strip indexed by i, the charge Q_i and its uncertainty σ_{Q_i} are obtained from the input charge profile. The cross-talk contribution to a neighboring strip j is calculated as:

$$C_{ij} = Q_i \times p_{ij} \qquad \text{4.6}$$

where p_{ij} is the cross-talk percentage from the predefined cross-talk map for the distance between strips i and j. The function updates the charge profile based on these calculations. The updated charge Q_i' at strip i after cross-talk application is:

$$Q_i' = Q_i + \sum_{\substack{k=1 \\ k \neq i}}^{N} (C_{ki} + C_{ik}) \qquad \text{4.7}$$

where C_{ki} represents the charge contributed from neighboring strip k to strip i, and C_{ik} is the charge that strip i contributes to its neighboring strip k. N is the total count of strips, and the summation iterates over all these strips. This formula accounts for the net charge redistribution due to cross-talk, considering both the charges received from and given to neighboring strips.

In order to set a mechanism for the charge sharing percentages, we adopt an exponential decay model. This model is predicated on the assumption that the charge sharing between any two strips, denoted as strip *i* and strip *j*, diminishes exponentially with the increasing distance between them and a decay scale. This decay law is justified by the physical nature of charge distribution in radiation detectors.

This exponential model is a reasonable approximation because the probability of a charge reaching a neighboring strip decreases with distance. The further away a strip *i* is from the charge deposited in strip *j*, the lower the probability that the charge at *i* will reach *j*. The function `chgCrossTalkExpLaw` defines the exponential decay law for charge sharing:

$$v_{\text{ChgShr}} = v_{\text{ChgShrNN}\,\%} \times e^{-\frac{d}{Scale}} \qquad \text{4.8}$$

This function generates an array of charge sharing percentages, v_{ChgShr}, starting from the initial sharing percentage for the nearest neighbors and decaying exponentially with distance d, then scaled according to the exponential law in μm, which can be varied along with the initial sharing percentage.

41

4.2.5 Front-end electronics effects

This step involves developing a module that simulates the process of converting analog signals from a detector into digital signals. This includes modeling the effects of noise, charge amplification and analog to digital conversion.

Noise Application

The function `applyNoise` applies a gaussian smearing of the input profile to simulate electronic noise. For each strip indexed by i, the function adds gaussian noise n_i with standard deviation σ_{Noise} to the charge Q_i collected at the strips. The noise is modeled as:

$$Q_{i(Chg+noise)} = Q_i + n_i, \quad n_i \sim \mathcal{N}(0, \sigma_{Noise}^2) \tag{4.9}$$

where $\mathcal{N}$ is a gaussian distribution with a mean equals to zero and a standard deviation σ_{Noise}^2. The uncertainty $\sigma_{i(new)}$ is given by:

$$\sigma_{i(new)} = \sqrt{\sigma_{Q_i}^2 + \sigma_{Noise}^2} \tag{4.10}$$

Charge Amplification

Following noise application, the function `applyAmplification` simulates charge amplification by scaling the charge profile by a gain factor $fGain$:

$$Q_{i(amp)} = Q_{i(Chg+noise)} \times fGain \tag{4.11}$$

It is important to note that gain is dimensionless, being the ration between the charge after amplification Q_{amp} and the charge collected Q_{coll}. Therefore, the result of a dimensionless number times the charge is clearly a charge, not a voltage.

Analog-to-Digital Conversion

The ADC process is simulated by the function `applyADC`, which discretize the amplified charge profile using a step function, the conversion is implemented as follows:

$$ADC_{counts} = \begin{cases} 0, & \text{if } Q_{i(amp)} < 0 \\ ADC_{max}, & \text{if } Q_{i(amp)} \geq fOlScale \\ \text{int}\left(\frac{Q_{i(amp)}}{OlScale} \times ADC_{max}\right), & \text{otherwise} \end{cases} \tag{4.12}$$

where $OlScale$ is the full scale range that the front-end electronics is capable of digitizing (in electron units) and maxADC is the maximum ADC count.

The `Pipeline` function sequentially applies noise, simulates cross-talk, amplifies the charge, and performs ADC conversion. The outcome of the digitizer module is profiles of ADC-counts of the detectors. The simulated charge profiles at each step are indicative of the detector's behavior under electronic effects, crucial for the optimization of detector systems.

4.3 Reconstruction of gamma beam profile

Once the profiles of ADC-counts in the detectors have been obtained, the next step is to fit the profiles with a gaussian model in order to reconstruct the profile of the electron/photon beam. This involves analyzing the fitted profiles of ADC-counts observables from each detector to determine the impacts of the the parameters defined in Subsections 4.2.3, 4.2.4, 4.2.5, 4.2.5 and 4.2.5.

The fit model is based on a gaussian function plus a baseline where this baseline is a polynomial of order zero (a constant), the fact that the beam gun is gaussian sets the underlying physics of what the detector should reconstruct. The model is characterized by its parameters: amplitude, mean, standard deviation and baseline. The function is expressed as:

$$f(x) = Ae^{-\frac{(x-\mu)^2}{2\sigma^2}} + B$$

<div align="right">4.13</div>

where A denotes the amplitude, μ is the mean, σ is the standard deviation, and B represents the baseline offset accounting for background contributions.

The baseline contribution within the fitting model is physically interpreted as arising from a small number of particles emanating from the direction of the beam. These particles constitute a low-level signal that must be accounted for in the fit to avoid any possible skewing the signal parameters.

The current fitting algorithms implemented in the module do not provide a robust solution for cases where the ADC profile is saturated. Saturation occurs when the signal exceeds the dynamic range of the detection system, leading to a

plateau in the ADC profile where the true signal peak is no longer distinguishable. This phenomenon poses a challenge for gaussian fitting. Hence, in the next sections, we explore and characterize the non-saturated region.

4.3.1 Optimization of detector digitization

The final step in the simulation pipeline is to optimize the digitization parameters of the detector by investigating the impacts of the phase parameters, where this "phase space" is not used in the traditional sense as it might be in physics. Instead, in this context, it is a term that encompasses the entire set of parameters that define the behavior and characteristics of the digitizer. This involves adjusting the charge collection efficiency, cross-talk charge sharing and front-end electronics parameters such as the electronic noise level, gain, full scale range and ADC resolution.

The optimization of the latter parameters requires sensible phase space values, in which the parameters are scanned across a range of values based on the FERS Characterization Report [82].

4.4 Simulation runs and analysis

In this section, we delve into the standalone simulation runs outputs and conditions. A detailed examination of the output analysis from these runs is then presented.

4.4.1 Electron beam run

Our goal in an electron beam run is to have an electron gaussian beam gun operating with an equivalent charge per bunch that is realistically tested in LUXE of 10^9 photons/Bx (where Bx represents a bunch). We first run the MC simulation for 10^6 photons and obtain the total energy deposited in the upstream sensor as 2.8×10^5 keV. Hence, the total energy deposited for 10^9 photons/Bx is predicted to be in the order of 2.8×10^8 keV. It is straightforward then to compute how many electrons would equalize the energy deposited since that the energy deposited of 1 electron is around 50 keV. Therefore, the total number of electrons that should be used for the run is 10^9, with 5×10^6 electrons/Bx for 200 bunches.

Since it would be computationally consuming to run the simulation with 10^9 electrons, we use a total number of electrons of 5×10^5. However, the ratio between the number of electrons per bunch and the number of bunches is compensated in the digitization pipeline by setting the number of electrons per bunch to 2500

(which means there is 200 bunches) and multiplying the CCE with a factor of 2000 to finally obtain the desired number of electrons per bunch of 5×10^6 electrons/Bx.

The initial conditions for the gaussian electron gun were set to an initial position vector of $(1, 1, -110)$ mm and a chosen standard deviation vector of $(2, 2, 0)$ mm. The resultant histogram, shown in Fig. 4.4, exhibits the horizontal charge deposition profile of the entire run, elucidating the spatial distribution of charges across the upstream and downstream sensors.
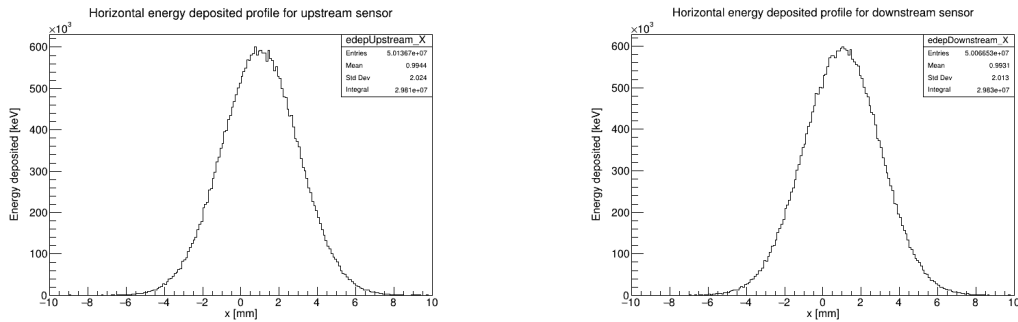
(A) Energy deposition profile for the entire run in the upstream sensor.

(B) Energy deposition profile for the entire run in the downstream sensor.

FIGURE 4.4 • The horizontal energy deposition profiles for both sensors.

The gaussian beam gun settings are further verified by capturing the longitudinal energy deposition profile. This profile is depicted in Fig. 4.5, where the electrons are minimum ionizing particle as we can observe by the energy deposited or dE/dz being constant along z.
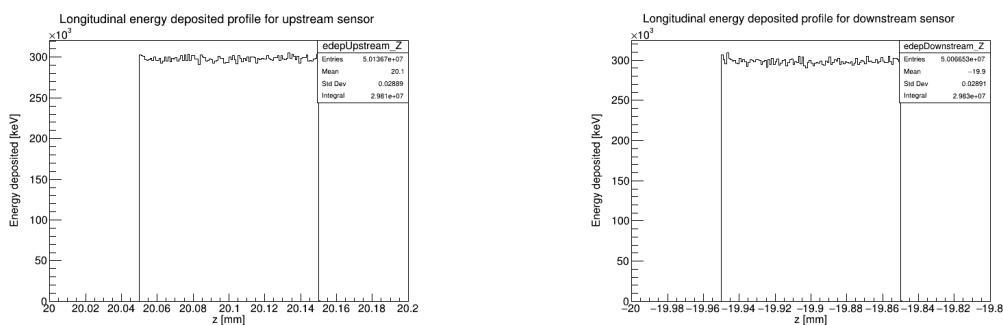
(A) Energy deposition profile in the upstream

(B) Energy deposition profile in the downstream

FIGURE 4.5 • The longitudinal energy deposition profiles for both sensors.

45

4.4.2 Digitizer pipeline verification histograms

To evaluate the digitizer response, the phase space parameters are plotted for one bunch in the entire run of the upstream sensor. To validate all the parameters, a simple pipeline run without a scan across the phase space parameters is executed with statistics of 1×10^5 e and 10000 e/Bx.

Tab. 4.1 displays the set of values chosen for verifying that the pipeline of digitization perform as expected.

Parameter	Value
Charge Collection Efficiency (CCE)	20%
Average Pair Energy	27.0 eV
Front-end Noise	5.18×10^4e
ADC Resolution	13-bits
Full Output Scale	1.12×10^7 e
Gain	5
Charge Sharing Cross-Talk Map	$[2\%, 100 \ \mu\mathrm{m}]$

TABLE 4.1 • Phase space parameters values for verification.

Starting from the deposition of charges from energy illustrated in Fig. 4.6, this charge is then collected in the electrodes of the sensors, as shown to the right in Fig. 4.6.
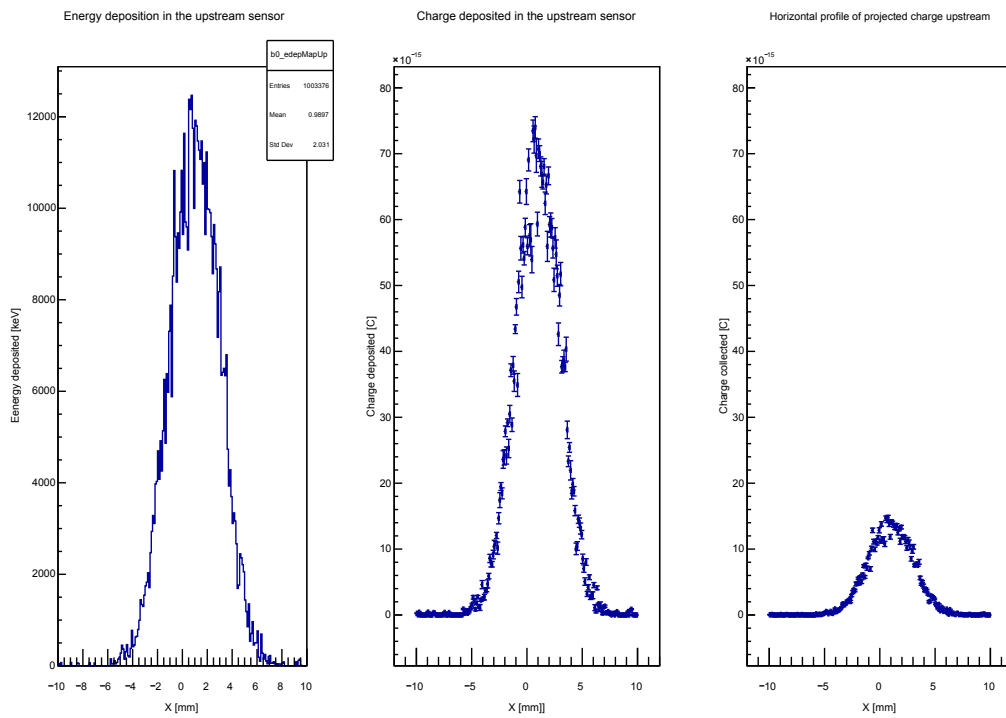
FIGURE 4.6 • Left: Energy deposited profile in the upstream sensor. **Middle:** Charge deposited profile. **Right:** Charge collected with $CCE = 20\%$ profile.

Front-end electronics effects are then applied to the charge collected profile with cross-talk effect. The first effect is the smeared noise which is set to a value of 5181 e as displayed in Fig. 4.7.
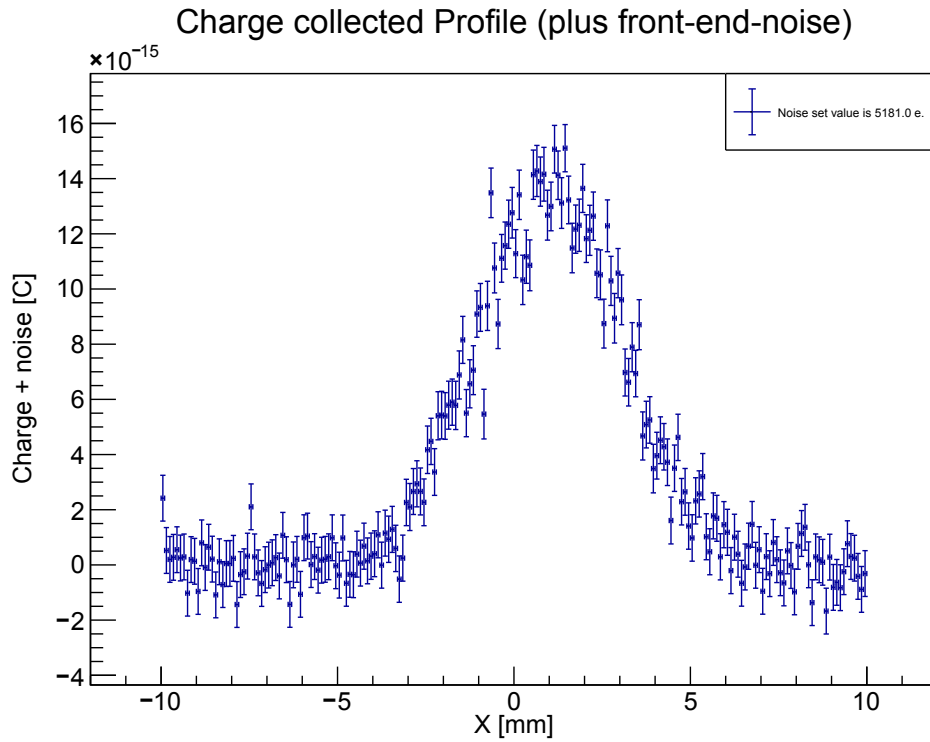
FIGURE 4.7 • Charge collected with the applied noise profile in the upstream sensor.

Afterwards, the strip cross-talk algorithm is applied to the collected charge profile, with a given vector for charge sharing percentages set as $[2\%, 100\ \mu\mathrm{m}]$, as shown in Fig. 4.8.
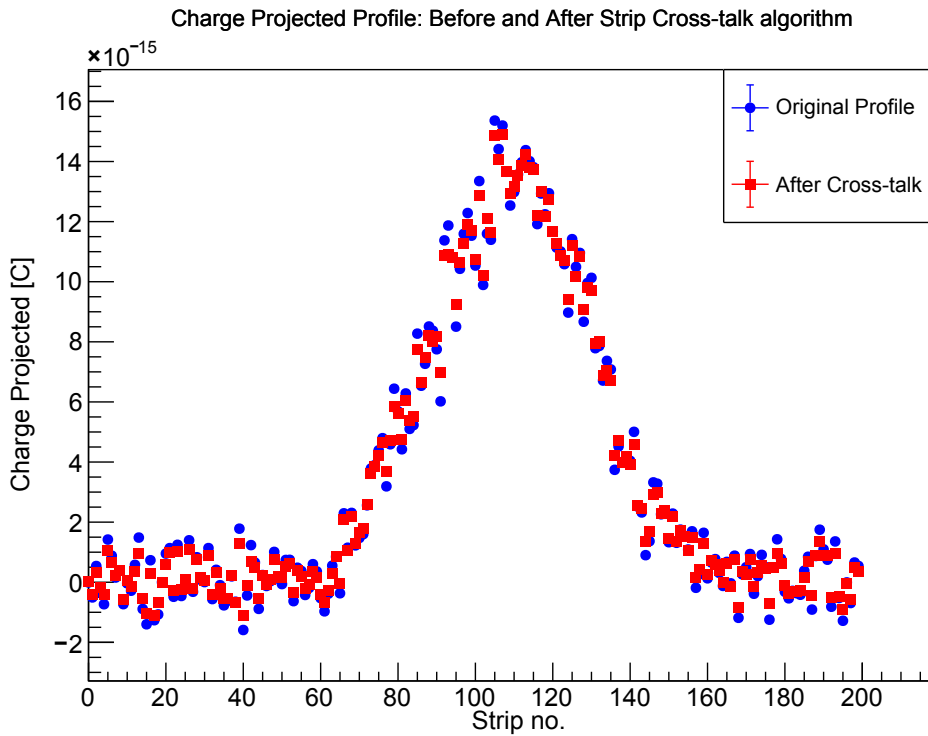
FIGURE 4.8 • Strip cross-talk effect before and after applying it to the charge collected profile in the upstream sensor.

The third effect is the amplification of the charge with the applied noise by multiplying it with the gain. This effect depicts the conversion of charge collected to amplified charge with a gain value set to 5.

The last effect is the Analog-to-Digitial Conversion, where $\text{OLSCALE} = 11.1875 \times 10^6$ e is the full scale range in units of electrons and $\text{MAXADC} = 2^{13} - 1$ is the maximum ADC count. The ADC count profile illustrated in Fig. 4.9 shows the result of conversion to digital counts.

Profile of ADC counts
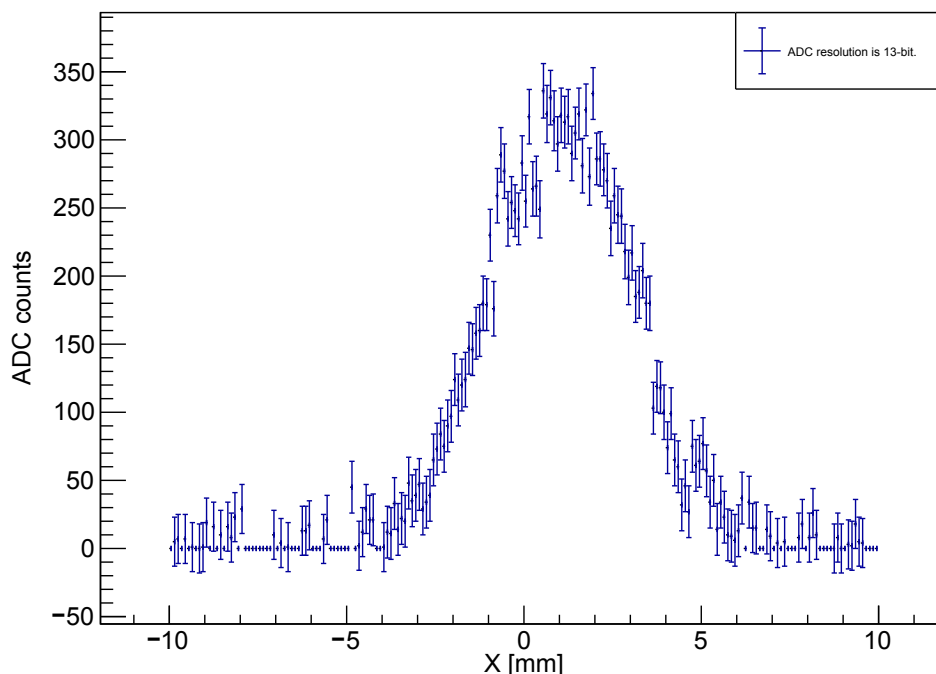
FIGURE 4.9 • ADC count profile in the upstream sensor.

4.4.3 Phase space parameters diagnostics histograms

In order to validate the phase space parameters steps in a scan, we use the following values for the scan steps:

Parameter	Value	Increment
Charge Collection Efficiency (CCE)	5% to 20%	2 steps
Average Pair Energy	Fixed @ 27.0 eV	–
Front-end Noise	5.180×10^4 to 9.134×10^4 e	10 steps
ADC Resolution	Fixed @ 13 bits	–
Full Output Scale	1.118×10^7 to 9.843×10^7 e	4 steps
Gain	5 to 63	4 steps
Charge Sharing Cross-Talk Map	[2%, 100 μm] to [10%, 100 μm]	2 steps

TABLE 4.2 • Phase space parameters scan.

The scan in Tab. 4.2 generates 640 files after the run. To affirm the scanned range for each parameter, we plot histograms for each sensor, which include the charge collection efficiency histogram as shown in Fig. 4.10a, noise level as depicted in Fig. 4.10b, the full-scale range in Fig. 4.11a, the gain in Fig. 4.11b, and the charge sharing cross-talk in Fig. 4.12.
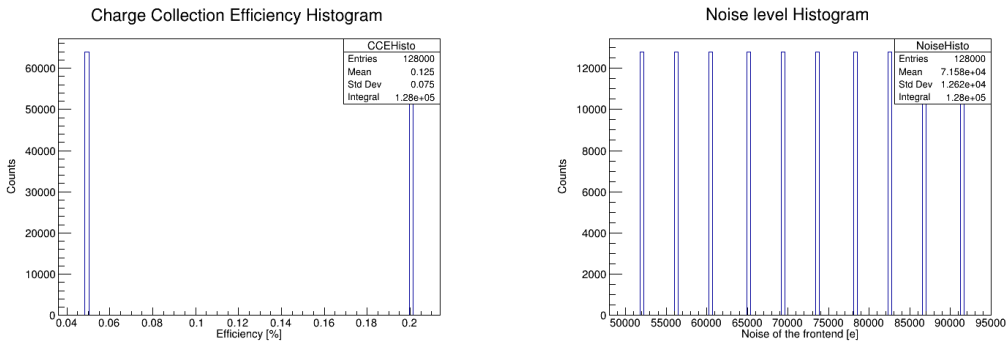
(A) Charge collection efficiency histogram.

(B) Noise level histogram in units of electrons.

FIGURE 4.10 • Histograms of the charge collection efficiency and noise level for both sensors.
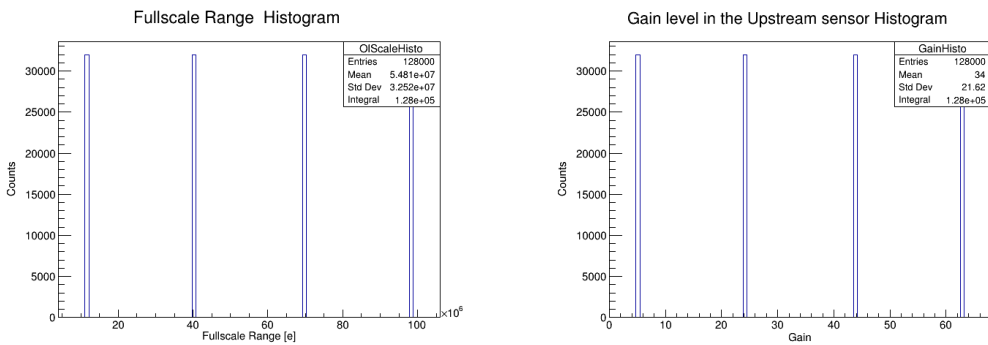
(A) Full scale range histogram in units of electrons.

(B) Gain level histogram.

FIGURE 4.11 • Histograms of the full scale range and gain level for both sensors.

51
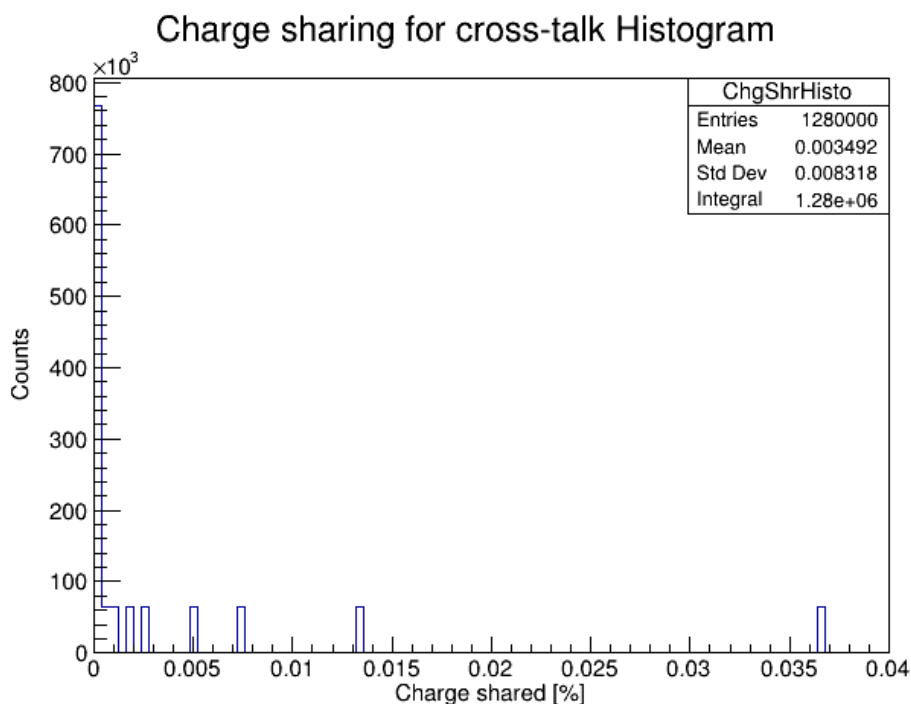
FIGURE 4.12 • The strip cross-talk charge shared in percent histogram for both sensors.

These histograms verify that the steps values for each of the phase space parameters are the same as the ones scanned in Tab. 4.2.

Observables diagnostics

The focal point of the analysis lies in the mean, standard deviation (sigma), amplitude and baseline derived from the gaussian model fit of the ADC count profile for both sensors across all bunches within the phase space scan.

Diagnostic histograms verify the gaussian beam gun conditions that are set in the MC simulation. Fig. 4.13 displays the histogram for amplitude obtained from the gaussian fit model.
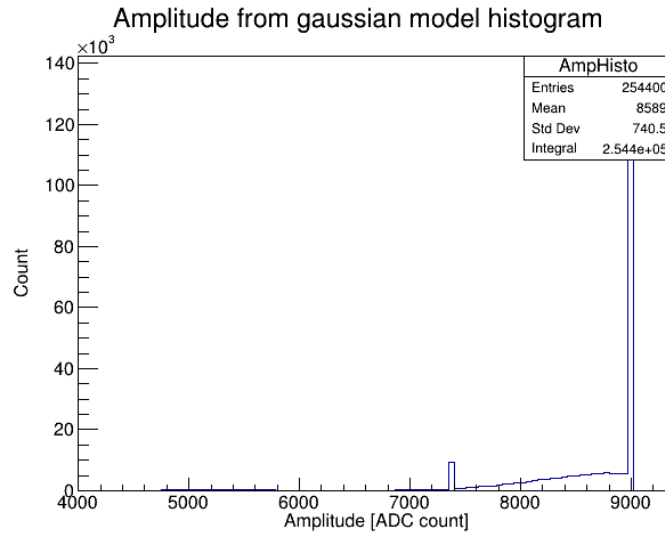
FIGURE 4.13 • Histogram of the amplitude observable.

In Fig. 4.13, we observe that the data is distributed around approximately 5550 and 7500 ADC counts. However, there is a peak around 9000, where ADC counts reach the highest value of 8191 counts. The latter reflects the fact that the ADC-count profiles fitted in this region are saturated.

Therefore, we first need to study the region of no-saturation in order to optimize the phase space parameters and eventually reconstruct the GBP resolution. Hence, the approach is to obtain the average and Root Mean Square (RMS) of the observables in order to measure the variability of such an observable.

4.4.4 Intrinsic detector response

Saturation occurs when the peak signal exceeds the detector's maximum ADC count, causing the ADC to plateau and, as a result, the signal's true peak to be obscured. This behaviour poses a problem for gaussian fitting.

Hence, our approach is to exclude the region of the parameters phase space where there is saturation of the ADC-count profiles. This is done in the digitizer script through a function that flags where there is a saturation or non-saturation in the ADC-count profiles and another function that writes in two separate .TXT files the parameters of which the latter happened. Finally, it returns observables values to zeros when saturation occurs.

Non-saturation electron beam run

The simulation is run with the same number of electrons per bunch and total number of electrons mentioned previously in Section 4.4. The most important parameters entering the saturation of the profiles are the CCE, full scale range and gain. Since the combination of the latter parameters are directly related to the digitization process, starting from the charge collection to ADC process, they are expected to produce saturation in the profiles.

The resultant set of non-saturation values for the phase space parameters is presented in Tab. 4.3.

Parameter	Value	Increment
Charge Collection Efficiency (CCE)	Fixed @ 5%	–
Average Pair Energy	Fixed @ 27.0 eV	–
Front-end Noise	5.180×10^4 to 9.134×10^4 e	10 steps
ADC Resolution	Fixed @ 13 bits	–
Full Output Scale	6.935×10^7 to 9.843×10^7 e	2 steps
Gain	Fixed @ 5	–
Charge Sharing Cross-Talk Map	[2%, $100 \ \mu$m] to [10%, $100 \ \mu$m]	2 steps

TABLE 4.3 • Non-saturation phase space parameters scan.

4.4.5 Optimization of Phase Space Parameters

To systematically analyze the impact of each phase space parameter on the fitting model observables, we adopted a methodical approach. By fixing all parameters with the values in Tab. 4.4 except one, we were able to scrutinize the variability of the observables—amplitude, mean, sigma, and baseline—relative to the parameter under investigation. Histograms for each observable are obtained as well.

Parameter	Value
Charge Collection Efficiency (CCE)	5%
Average Pair Energy	27.0 eV
Front-end Noise	5.180×10^4 e
ADC Resolution	13 bits
Full Output Scale	9.843×10^7 e
Gain	5
Charge Sharing Cross-Talk Map	[2%, $100 \ \mu$m]

TABLE 4.4 • The fixed phase space parameters values.

Non-Saturation Analysis

Here, we analyze two types of graphs: (1) diagnostic histograms for each of the observables, and (2) plots of the average of the observables. It is important to note that the averages and RMS values of the averages are computed following the methodical approach mentioned previously. Then, the observables as a function of each parameter steps in Tab. 4.3 are plotted.

In Fig. 4.14a, Fig. 4.14b, Fig. 4.15a, and Fig. 4.15b, the histograms for the amplitude, mean, sigma, and baseline are shown respectively.
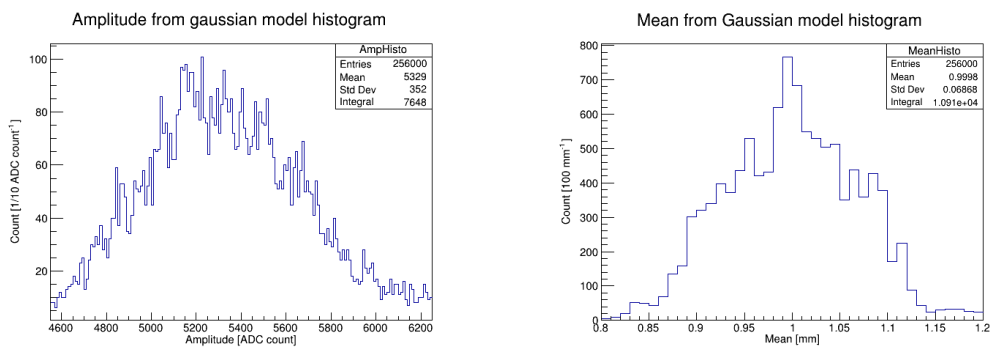
(A) Histogram of the amplitude observable.   **(B)** Histogram of the mean observable.

FIGURE 4.14 • Histograms of the amplitude and mean observables in the no-saturation phase space scan.

The amplitude histogram displayed in Fig. 4.14a shows the distribution of amplitude values around 5329 ADC counts. It is expected that the amplitude values should be less than the maximum ADC count. The mean histogram in Fig. 4.14b shows a distribution around $1 \, \mathrm{mm}$. The resulting mean value in the distribution reflects the fact that the value of mean that is set in the conditions of the gaussian electron beam gun of the run, which is correct.
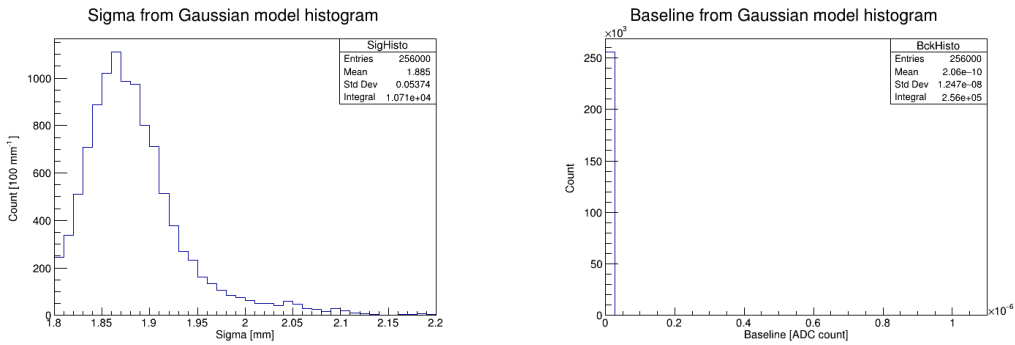
(A) Histogram of the sigma observable.

(B) Histogram of the baseline observable.

FIGURE 4.15 • Histograms of the mean and baseline observables in the no-saturation phase space scan.

The sigma histogram in Fig. 4.15a illustrates a distribution around $1.8\,\mathrm{mm}$. Noteworthy, the expected sigma value that is set in the conditions of the gaussian electron beam of the run is $2\,\mathrm{mm}$, which suggests that there could be a systematic error. The baseline histogram depicted in Fig. 4.15b is attributed to the polynomial added to the gaussian fit model and arises from a small number of particles emanating from the direction of the beam. It is evident that the baseline values are in the order of 10^{-10} ADC count.

Here, we show: (2) the average for each observable and sigma error as a function of phase space parameters, which are the noise level and full scale range across the scan steps in Tab. 4.3. Note that the figures for the observables as a function of charge collection efficiency and gain are omitted because they only contain one point that represents the step value mentioned in Tab. 4.3.
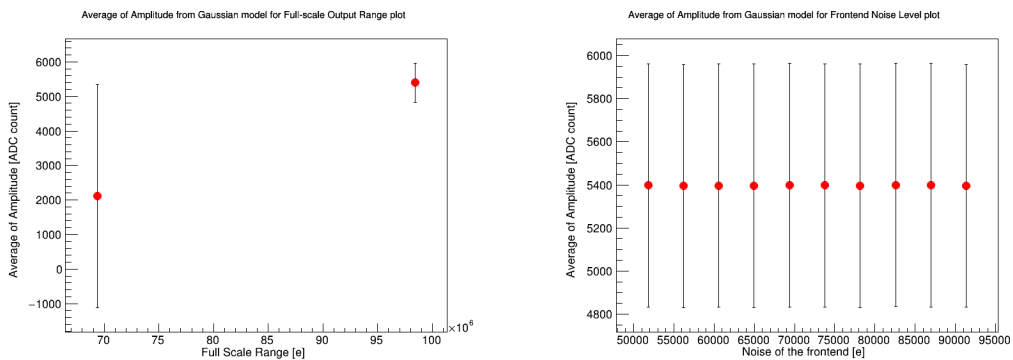
(A) Average of amplitude observable as a function of the full scale range parameter.

(B) Average of amplitude observable as a function of noise level parameter.

FIGURE 4.16 • Average plots for amplitude observable as a function of full scale range and noise parameters, the uncertainty of each point is the RMS value.

For the full scale range parameter in Fig. 4.16a, we notice that the uncertainty in the first point has a larger magnitude compared to the second point. This reflects the fact that the range of digitiztion is larger than the first point value. Hence, the second point value yields an amplitude value that is in a normal distribution, evident from Fig. 4.14a. As for the noise parameter in Fig. 4.16b, it is expected that the amplitude values and uncertainties across the noise levels have close values to each other.
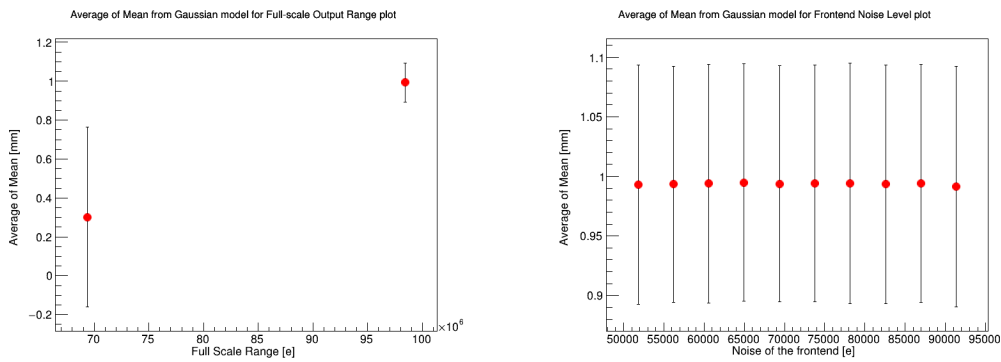
(A) Average of mean observable as a function of the full scale range parameter.

(B) Average of mean observable as a function of the noise parameter.

FIGURE 4.17 • Average plots for mean observable as a function of the full scale range and noise parameters, the uncertainty of each point is the RMS value.

For the full scale range parameter in Fig. 4.17a, we already mentioned that the first point value of the full scale range doesn't represent the digitizer range, in this plot, it confirms it that again since the mean value is 0.3 mm. However, the second point has a value of 1 mm, which reflects the mean value that is set in the electron gaussian beam gun conditions. As for the noise parameter in Fig. 4.17b, the mean values and uncertainties are in the proximity of each other with the expected value of 1 mm. Hence, the noise level doesn't seem to affect the mean values.

57
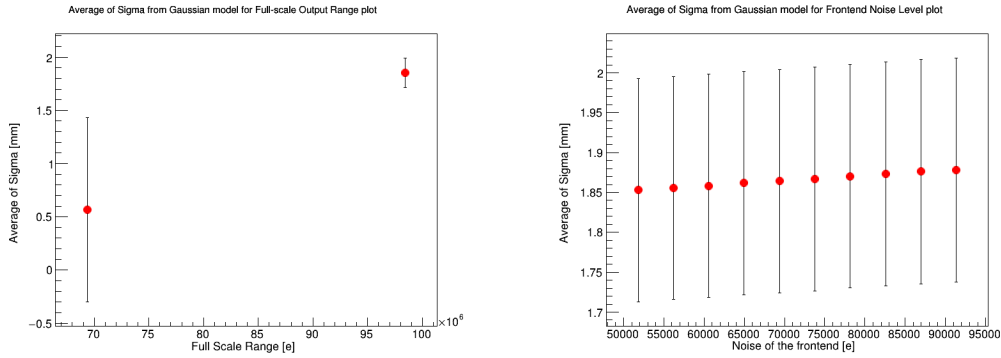
(A) Average of sigma observable as a function of the full scale range parameter.

(B) Average of sigma observable as a function of the noise parameter.

FIGURE 4.18 • Average plots for sigma as a function of full scale range and noise parameters, the uncertainty of each point is the RMS value.

For the full scale range parameter in Fig. 4.18a, the second point has a sigma value of 1.8 mm which is inconsistent with the sigma value that is set in the electron gaussian beam conditions of 2 mm. This inconsistency suggests that there could be a systematic error in the data that should be investigated. As for the noise parameter in Fig. 4.18b, the sigma values show a slight linear increase (in the order of $25\ \mu$m). The closest value to the sigma that is set in the electron beam gun run is found at 9.134×10^4 e which reflects the fact that the noise being applied is gaussian.
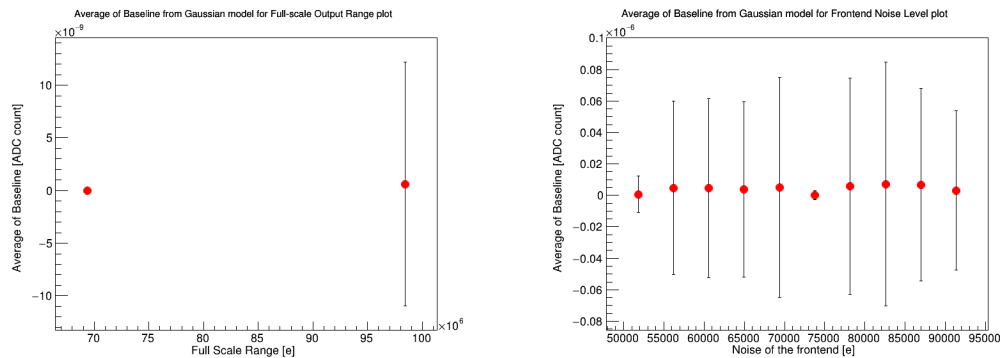
(A) Average of baseline observable as a function of the full scale range parameter.

(B) Average of baseline observable as a function of the noise parameter.

FIGURE 4.19 • Average plots for baseline observable as a function of full scale range and noise parameters, the uncertainty of each point is the RMS value.

For the full scale range parameter in Fig. 4.19a, the second point only has a baseline value which indeed doesn't affect the fit model as its value is in the order of 10^{-9} ADC count. As for the noise parameter in Fig. 4.19b, the baseline values

and uncertainties don't reflect any effect with the increase of the noise level. As expected in general, their values are considered negligble, due to the insignificant number of particles emanating from the direction of the beam.
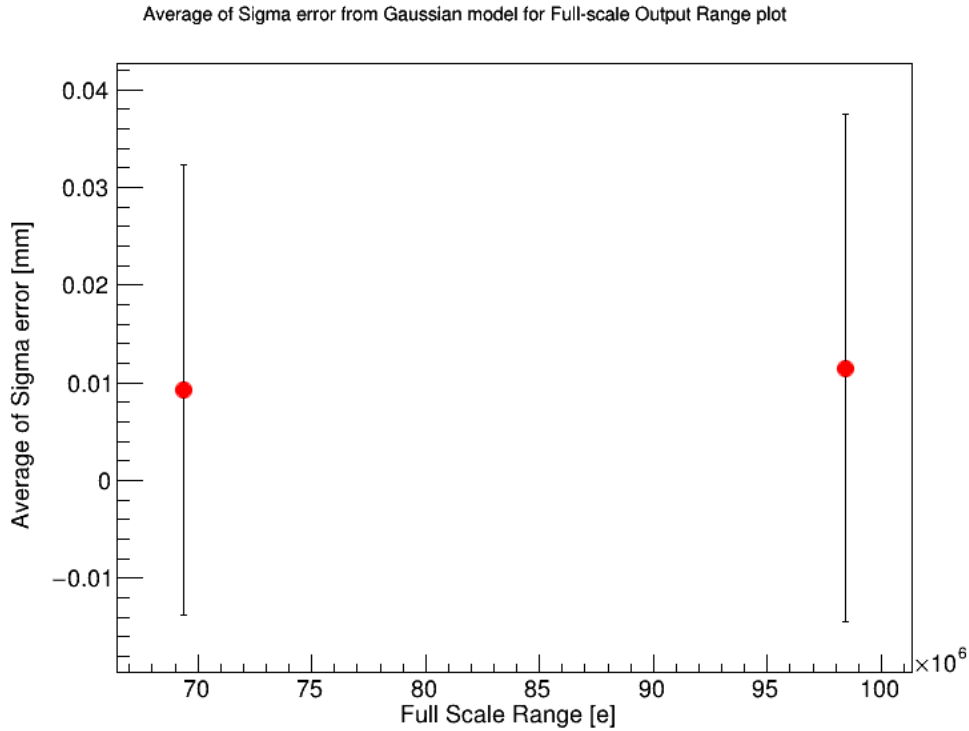
FIGURE 4.20 • Average plot for sigma error as a function of full scale range parameter, the uncertainty of each point is the RMS value.

Lastly, we show the full scale range parameter in Fig. 4.20, we notice that the RMS of the sigma error increases about $3~\mu\mathrm{m}$ from the first point to the second, which reflects the fact that the increase of the full scale range doesn't affect the sigma error significantly. However, increasing the full scale range affects the amplitude, mean and sigma evident in Fig. 4.16a, Fig. 4.17a and Fig. 4.18a, respectively.

Therefore, in the non-saturation region of the phase space parameters, we elucidate that the average RMS of the sigma error, i.e. the GBP resolution, is around $24.5~\mu\mathrm{m}$. This spatial resolution is a result of choosing the values of the phase space parameters found in Tab. 4.4. These selected values are the optimal values of the phase space parameters. Hence, changing the values selected would result in a change of the resolution value.

GBP beam test

5.1 Sapphire sensors as GBP

This chapter discusses the development and testing of sapphire sensors for Gamma Beam Profiling, specifically focusing on "sapphire pads," "sapphire 4-strip," and "sapphire 192 micro-strip" prototypes. It covers the beam test at CERN's CLEAR of the third prototype. The chapter also addresses the data acquisition and analysis systems, including the use of the Trigger Logic Unit for synchronization. Key points include resolution analysis strategies and data correlation between different sensors, supported by graphical data representations.

The first version of sapphire sensors, designated as "sapphire pads", were tested in May '22 at BTF (INFN-Frascati). The test involved two sapphire pad detectors (with diameters of 1.6 mm and 5.5 mm, and thicknesses of 110 μm and 150 μm, respectively). They were subjected to a 300 MeV electron beam with an intensity of up to 33×10^{10} e$^-$/s. The main goal of these tests was to analyze the collected charge based on parameters like voltage and beam charge. These pad sensors, possess a geometric blueprint that allows the entirety of the beam to be contained within the pad. Fig. 5.1 displays the sapphire pad sensor tested at INFN-Frascati.

FIGURE 5.1 • Sapphire pads tested at INFN-Frascati.

The "sapphire 4-strip" sensors, released in September '22 and tested at CLEAR (CERN), comprised three 4-strip detectors of diverse thicknesses. These sensors emphasized understanding aspects like radiation damage and signal uniformity. The design of the 4-strip sensors can be observed in Fig. 5.2.

FIGURE 5.2 • The Sapphire 4-strip sensor that was tested at CLEAR (CERN).

By December '22, the "sapphire 192 micro-strip" sensors came into the fold. Which was tested at CLEAR (CERN) and featured the CAEN FERS electronics capable of reading out 64 strips. This model delved into areas such as electronics integration and charge collection. The design of the sensor is shown in Fig. 5.3.
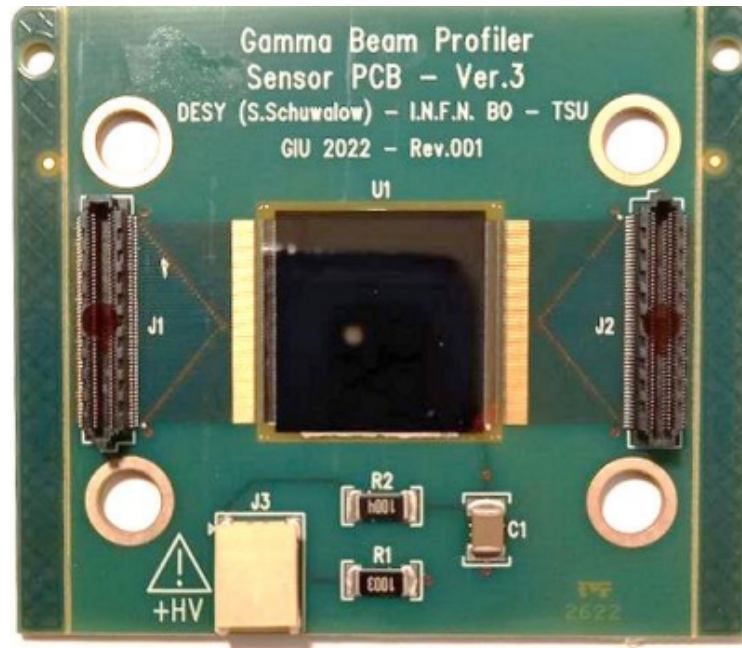
FIGURE 5.3 • The Sapphire 192-strip sensor that was tested at CLEAR (CERN).

Each microstrip has a size of 0.08×20 mm^2 and a pitch of 0.1 mm, which means that they are spaced at a distance of 0.02 mm from each other.

The two thicknesses of the sensor are 110 and 150 μm, depending on the specific application, and its overall size is 22×23 mm^2. The active area of the sensor, where the particles or photons are detected, is 20×19.2 mm^2. The 192 micro-strips sensor is shown in Fig. 5.4.

(a)

Al (1μm)

Cr (60 nm)

Sapphire

Cr/Ni (20/200 nm)

(b)

FIGURE 5.4 • (a) A close up perspective of the 192 microstrips sensor. **(b)** Sensor contact structure [3]

The back-plane contact of the sensor is designed for high voltage bias, which means that a voltage difference is applied between the microstrips and the back-plane to create an electric field in order to collect the charge carriers generated by the incident radiation. The dimensions of the back-plane contact are $20 \times 21 \ \mathrm{mm}^2$, which provides a large area for the electrical connection and reduces the resistance of the circuit.

To mount the sensor on a printed circuit board (PCB), epoxy glue is used to ensure a strong and reliable bond between the two surfaces. Moreover, The PCB is $60 \times 60 \ \mathrm{mm}^2$ in overall size.

5.2 GBP resolution analysis

GBP resolution analysis strategy is: for each event, the data of the FERS is synchronized with the camera:

→ this is done by selecting the `det1strip96` charge and the `profile_amp_hor` from camera. The two quantities are correlated in time with the beam charge;

→ correlation between the two normalized signals (`sig/std`) is calculated and offset between the two (t, Q_{s96d1}) and (t, Q_{camera}) in trigger offset is obtained;

→ the camera's timestamp is attached in the 'time' branch of the FERS data - i.e., creating a map between the event of the FERS and those of the Basler.

For each event, it is calculated:

→ charge profile (Gaussian + constant) fit of odd/even/full profiles → $(A, x_0, \sigma)_{\text{odd,even,full}}$

→ the scatter plot between the beam charge $Q \propto A\sigma$ of detector and camera → inspect synchronization

→ the ratio between σ_{det} and σ_{camera}

Synchronization example with run45 from March data is shown in Fig. 5.5, Correlation with detector charge (from det1 strip96) and basler horizontal amplitude is used to determine the offset between the two sets (in Fig. 5.5).
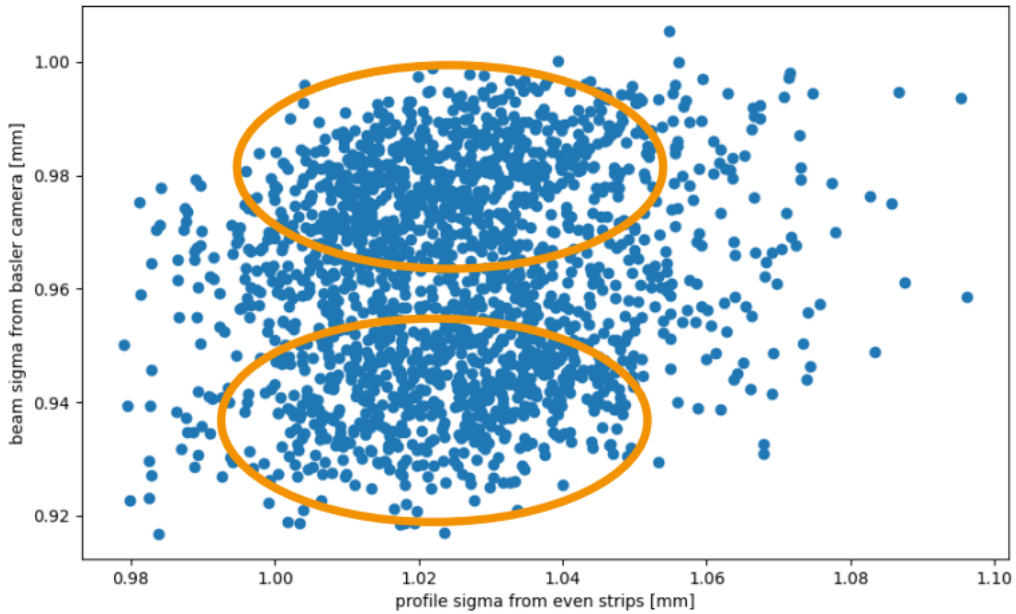
FIGURE 5.5 • Profile of sigma from even strips versus beam sigma from balser camera to show correlation with detector charge (from det1 strip96) and basler horizontal amplitude

The GBP resolution is estimated from the difference between the sigma from det0 and from det1 sigma:

$$var \equiv (\sigma_{d0} - \sigma_{d1}) \qquad\qquad 5.1$$

$$\delta var = \sqrt{\delta\sigma_{d0} + \delta\sigma_{d1}} \approx \sqrt{2}\delta\sigma_{GBP} \qquad 5.2$$

assuming that

$$\delta\sigma_{\text{det0}} = \delta\sigma_{\text{det1}} = \delta(\sigma_{d0} - \sigma_{d1})/\sqrt{2} \qquad 5.3$$

It is important to note that the even/odd strips are treated separately. Plots showing the difference between the sigma inferred from upstream and the one from downstream sensors for run45 and run69 are in Fig. 5.6a and Fig. 5.6b.
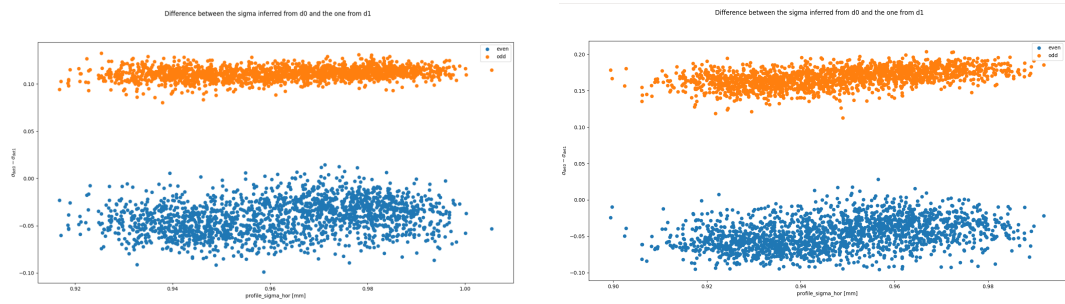
(A) Run45 plot of difference between the profile sigma versus the difference between the sigma from d0 and d1.

(B) Run69 plot of difference between the profile sigma versus the difference between the sigma from d0 and d1.

FIGURE 5.6 • Plots displaying the difference between the profile sigma versus the difference between the sigma inferred from d0 and d1 of run45 and run69.

We obtain from the previous plots the following resolutions from run45 (from even = 12.9 μm and a resolution from odd = 4.2 μm) and from run69 (from even = 14.9 μm and a resolution from odd = 8.5 μm). Therefore, if we sum the resolutions from odd and even strips, we obtain from run45 a resolution of 17.1 μm and from run69 a resolution of 23.4 μ.

In Chapter 6 we compare the GBP resolution obtained from the standalone MC simulation in Chapter 4 and the resolutions obtained from run45 and run69 in this chapter.

Discussion

In this section, we firstly consider the parametric influence that was applied to the Gaussian model. Secondly, we comparatively discuss the results of the GBP beam test that was elaborated in Chapter 5 and the results obtained from the standalone MC simulation that was explained in Chapter 4.

6.1 Parametric Influence on the Gaussian model

The baseline component identified in the Gaussian fit encapsulates more than just electronic noise and signal fluctuations; it bears the signature of physical processes intrinsic to the experimental setup. Specifically, this baseline is attributed to secondary particles that emerge from interactions with the Kapton window situated in the beam's path. These particles, while not part of the primary beam signal, contribute to the signal measured by the detectors and are superimposed on the primary beam profile.

In the Geant4 Monte Carlo simulations, this baseline is reflected as a low-intensity baseline in the reconstructed energy deposition profile. As the beam traverses the Kapton window, secondary particles are produced, leading to additional energy depositions that form a discernible baseline in the detectors' response. Consequently, the Gaussian fit employed to deduce the beam profile must account for these secondary contributions to accurately characterize the beam's properties.

6.2 Insights from Beam Test

The experimental data from March CERN @ CLEAR run, as mentioned in Chapter 5, provide a crucial empirical foundation for the simulation outcomes. The GBP resolutions obtained from run45 and run69 are the sum of the resolutions from odd and even strips, which are 17.1 μm and 23.4 μ, respectively, resulting in an average of approximately 20.25 μm.

6.2.1 Comparison of Experimental and Simulation Results

A comparison between the experimental results from the March CERN @ CLEAR beam test and the simulation outcomes reveals a noteworthy correlation in terms of the order of magnitude. The average GBP resolution reconstructed using a Gaussian model is determined to be 24.5 μm. The difference between the average experimental and simulation resolutions is 4.25 μm

The percentage difference between the experimental and simulation results for the GBP resolution is approximately 17.35%. This value is calculated by comparing the absolute difference between the experimental average resolution (20.25 μm) and the simulation resolution (24.5 μm) with respect to the simulation resolution.

A 17.35% difference indicates a notable variance, suggesting that while the simulation and experimental results are closely aligned in terms of order of magnitude, there are disparities that could be due to experimental uncertainties, environmental conditions during the tests, or limitations within the simulation model itself. However, the close proximity of these values, especially considering the complexities involved in high-precision measurements, underscores the robustness of the simulation framework. This congruence is pivotal for future experimental planning, as it provides a reliable predictive model for the GBP response under various experimental conditions.

Conclusions

The LUXE (Laser Und XFEL Experiment) at DESY Hamburg is a pioneering initiative in Quantum Electrodynamics (QED), leveraging the European XFEL's electron beam and an ultra-high intensity optical laser. Its goal is to probe the non-perturbative regime of QED and search for new particles that couple to photons. LUXE experimental configurations involve directing the XFEL electron beam through a high-intensity laser focus and interacting a high-energy photon beam with the laser.

The GBP, a novel Sapphire detector, is central to LUXE, tasked with measuring the spatial distribution of gamma-ray photons. Its design, developed for precision and radiation hardness, allows it to operate under intense gamma-ray fluxes.

Our detailed exploration of the phase space parameters in the context of GBP, as documented in Chapter 4 and 6, has led to understanding of the parameters' behavior and the reconstruction of GBP resolution.

The analysis revealed that ADC saturation posed a major challenge, obscuring the true peak of signals and hindering the Gaussian fitting process. By excluding the saturation-affected regions from the parameter space, as outlined in Table 4.3 in Chapter 4, we isolated a set of non-saturation parameters for our study.

Through a systematic approach of varying individual phase space variables while keeping others constant (see Table 4.4 in Chapter 4), we meticulously analyzed the effect of each parameter on key observables: amplitude, mean, sigma, and sigma error. This analysis not only provided clarity on the behavior of these observables but also allowed us to pinpoint the optimal parameters values for the GBP.

A pivotal outcome of our research was the determination of the final GBP resolution. In the non-saturation region of the phase space parameters, the average RMS of the

sigma error — essentially the GBP resolution — was found to be $24.5\ \mu$m. This resolution is a direct result of the selected values in Table 4.4 in Chapter 4.

Additionally, the mean observable value in the non-saturation region was observed to be in precise agreement with the predefined conditions of the electron beam run. However, for the sigma observable, its value of around $1.8\ \mu$m suggests that there could be a systematic error in the data that needs to be further investigated.

The GBP beam test at CLEAR in March 2023 was pivotal for analyzing the GBP resolution, with results indicating resolutions of $17.1\ \mu$m and $23.4\ \mu$m, for run45 and run69 respectively, averaging to approximately $20.25\ \mu$m. This detailed analysis, as described in Chapter 5, was integral to understanding GBP performance.

In comparison, the average GBP resolution from MC simulation, discussed in Chapter 4, was $24.5\ \mu$m, aligning with the experimental results in terms of magnitude (10^1 or tens of micrometers). The discrepancy of around $4.25\ \mu$m which results in a difference percentage of 17.35% between the experimental average and the simulation may be attributed to factors like experimental conditions and detector complexities, but it highlights the robustness and reliability of the simulation framework. Therefore, these factors need to be investigated furthermore to underline the reasons.

List of Figures

73

List of Tables

Bibliography

[1] H. Abramowicz and U. Acosta and M. Altarelli and R. Aßmann and Z. Bai and T. Behnke and Y. Benhammou and T. Blackburn and S. Boogert and O. Borysov and M. Borysova and R. Brinkmann and M. Bruschi and F. Burkart and K. Büßer and N. Cavanagh and O. Davidi and W. Decking and U. Dosselli and N. Elkina and A. Fedotov and M. Firlej and T. Fiutowski and K. Fleck and M. Gostkin and C. Grojean and J. Hallford and H. Harsh and A. Hartin and B. Heinemann and T. Heinzl and L. Helary and M. Hoffmann and S. Huang and X. Huang and M. Idzik and A. Ilderton and R. Jacobs and B. Kämpfer and B. King and H. Lahno and A. Levanon and A. Levy and I. Levy and J. List and W. Lohmann and T. Ma and A. J. Macleod and V. Malka and F. Meloni and A. Mironov and M. Morandin and J. Moron and E. Negodin and G. Perez and I. Pomerantz and R. Pöschl and R. Prasad and F. Quéré and A. Ringwald and C. Rödel and S. Rykovanov and F. Salgado and A. Santra and G. Sarri and A. Sävert and A. Sbrizzi and S. Schmitt and U. Schramm and S. Schuwalow and D. Seipt and L. Shaimerdenova and M. Shchedrolosiev and M. Skakunov and Y. Soreq and M. Streeter and K. Swientek and N. Tal Hod and S. Tang and T. Teter and D. Thoden and A. I. Titov and O. Tolbanov and G. Torgrimsson and A. Tyazhev and M. Wing and M. Zanetti and A. Zarubin and K. Zeil and M. Zepf and A. Zhemchukov. Conceptual design report for the LUXE experiment. *The European Physical Journal Special Topics*, 230(11):2445–2560, 2021. (Cited on pages 1, 13, and 16.)

[2] Ruth Jacobs. Luxe: A new experiment to study non-perturbative qed in e^-−laser and γ-laser collisions. *SciPost Physics Proceedings*, (8):088, 2022. (Cited on pages 1 and 2.)

[3] John Andrew Hallford. Detector challenges at the luxe experiment, 2022. (Cited on pages 2, 64, and 73.)

[4] Paul Adrien Maurice Dirac. The quantum theory of the emission and absorption of radiation. *Proceedings of the Royal Society of London. Series A, Containing Papers of a Mathematical and Physical Character*, 114(767):243–265, 1927. (Cited on page 3.)

[5] R. P. Feynman. Mathematical formulation of the quantum theory of electro-magnetic interaction. *Phys. Rev.*, 80:440–457, Nov 1950. (Cited on page 3.)

[6] D Hanneke, S Fogwell Hoogerheide, and G Gabrielse. Cavity control of a single-electron quantum cyclotron: Measuring the electron magnetic moment. *Physical Review A*, 83(5):052122, 2011. (Cited on pages 4 and 5.)

[7] Tatsumi Aoyama, Toichiro Kinoshita, and Makiko Nio. Theory of the anomalous magnetic moment of the electron. *Atoms*, 7(1):28, 2019. (Cited on page 4.)

[8] Léo Morel, Zhibin Yao, Pierre Cladé, and Saïda Guellati-Khélifa. Determination of the fine-structure constant with an accuracy of 81 parts per trillion. *Nature*, 588(7836):61–65, 2020. (Cited on page 4.)

[9] A Fedotov, A Ilderton, F Karbstein, Ben King, D Seipt, H Taya, and Greger Torgrimsson. Advances in qed with intense background fields. *Physics Reports*, 1010:1–138, 2023. (Cited on page 4.)

[10] Remo Ruffini, Gregory Vereshchagin, and She-Sheng Xue. Electron–positron pairs in physics and astrophysics: from heavy nuclei to black holes. *Physics Reports*, 487(1-4):1–140, 2010. (Cited on pages 4 and 6.)

[11] AI Nikishov. Absorption of high energy photons in the universe. *Zhur. Eksptl'. i Teoret. Fiz.*, 41, 1961. (Cited on page 4.)

[12] Chryssa Kouveliotou, S Dieters, T Strohmayer, J Van Paradijs, GJ Fishman, CA Meegan, K Hurley, J Kommers, I Smith, D Frail, et al. An x-ray pulsar with a superstrong magnetic field in the soft γ-ray repeater sgr1806- 20. *Nature*, 393(6682):235–237, 1998. (Cited on page 4.)

[13] Alice K Harding and Dong Lai. Physics of strongly magnetized neutron stars. *Reports on Progress in Physics*, 69(9):2631, 2006. (Cited on page 4.)

[14] Roberto Turolla, Silvia Zane, and AL Watts. Magnetars: the physics behind observations. a review. *Reports on Progress in Physics*, 78(11):116901, 2015. (Cited on pages 4 and 8.)

[15] V Yakimenko, S Meuren, F Del Gaudio, C Baumann, A Fedotov, F Fiuza, T Grismayer, MJ Hogan, A Pukhov, LO Silva, et al. Prospect of studying nonperturbative qed with beam-beam collisions. *Physical review letters*, 122(19):190404, 2019. (Cited on page 4.)

[16] Phil H Bucksbaum, Gerald V Dunne, Frederico Fiuza, Sebastian Meuren, Michael E Peskin, David A Reis, Greger Torgrimsson, Glen White, and Vitaly Yakimenko. Probing qed cascades and pair plasmas in laboratory experiments loi to cosmic frontier. Snowmass, 2021. (Cited on page 4.)

[17] Sh Zh Akhmadaliev, G Ya Kezerashvili, SG Klimenko, RN Lee, VM Malyshev, AL Maslennikov, AM Milov, AI Milstein, N Yu Muchnoi, AI Naumenkov, et al. Experimental investigation of high-energy photon splitting in atomic fields. *Physical review letters*, 89(6):061802, 2002. (Cited on page 4.)

[18] Misha Yu Ivanov, Michael Spanner, and Olga Smirnova. Anatomy of strong field ionization. *Journal of Modern Optics*, 52(2-3):165–184, 2005. (Cited on page 4.)

[19] W Heisenberg and H Euler. Consequences of dirac theory of the positron. *arXiv preprint physics/0605038*, 2006. (Cited on page 6.)

[20] Roberto Iengo and Marco Serone. A simple uv completion of qed in 5 dimensions. *Physical Review D*, 81(12):125005, 2010. (Cited on page 6.)

[21] Ursula Keller. Recent developments in compact ultrafast lasers. *nature*, 424(6950):831–838, 2003. (Cited on page 6.)

[22] Thomas Brabec and Ferenc Krausz. Intense few-cycle laser fields: Frontiers of nonlinear optics. *Reviews of Modern Physics*, 72(2):545, 2000. (Cited on page 6.)

[23] A Ilderton. Note on the conjectured breakdown of qed perturbation theory in strong fields. *Physical Review D*, 99(8):085002, 2019. (Cited on page 7.)

[24] Laurent Canetti, M. Drewes, T. Frossard, and M. Shaposhnikov. Dark matter, baryogenesis and neutrino oscillations from right handed neutrinos. *Physical Review D*, 87:1–36, 2012. (Cited on page 8.)

[25] DM Volkov. On a class of solutions of the dirac equation. *Z. Phys*, 94(3-4):250–260, 1935. (Cited on page 8.)

[26] Chris Harvey, Thomas Heinzl, and Anton Ilderton. Signatures of high-intensity compton scattering. *Physical Review A*, 79(6):063407, 2009. (Cited on page 9.)

[27] Anthony Hartin, Andreas Ringwald, and Natalia Tapia. Measuring the boiling point of the vacuum of quantum electrodynamics. *Physical Review D*, 99(3):036008, 2019. (Cited on page 11.)

[28] So V Bulanov, NM Naumova, and Francesco Pegoraro. Interaction of an ultrashort, relativistically strong laser pulse with an overdense plasma. *Physics of Plasmas*, 1(3):745–757, 1994. (Cited on page 11.)

[29] Roland Lichters, J Meyer-ter Vehn, and A Pukhov. Short-pulse laser harmonics from oscillating plasma surfaces driven at relativistic intensity. *Physics of Plasmas*, 3(9):3425–3437, 1996. (Cited on page 11.)

[30] Brendan Dromey, Daryl Adams, R Hörlein, Y Nomura, SG Rykovanov, DC Carroll, PS Foster, Satyabrata Kar, Keith Markey, P McKenna, et al. Diffraction-limited performance and focusing of high harmonics from relativistic plasmas. *Nature Physics*, 5(2):146–152, 2009. (Cited on page 11.)

[31] Richard H Milburn. Electron scattering by an intense polarized photon field. *Physical Review Letters*, 10(3):75, 1963. (Cited on page 11.)

[32] VI Ritus. Vacuum polarization correction to elastic electron and muon scattering in an intense field and pair electro-and muoproduction. *Nuclear Physics B*, 44(1):236–252, 1972. (Cited on page 12.)

[33] Huayu Hu, Carsten Müller, and Christoph H Keitel. Complete qed theory of multiphoton trident pair production in strong laser fields. *Physical review letters*, 105(8):080401, 2010. (Cited on page 12.)

[34] Anton Ilderton. Trident pair production in strong laser pulses. *Physical review letters*, 106(2):020404, 2011. (Cited on page 12.)

[35] T. G. Blackburn. Ptarmigan. (Cited on page 13.)

[36] Matthew McCullough. Lectures on physics beyond the standard model. *6th Tri-institute summer school on elementary particles*, 5, 2018. (Cited on page 13.)

[37] Richard Keith Ellis, Marco Sozzi, Aleandro Nisati, Monica D'Onofrio, Ferenc Siklér, Daniel Schulte, Jorgen D'Hondt, Joerg Jaeckel, Matthew McCullough, Urs Wiedemann, et al. Physics briefing book: input for the european strategy for particle physics update 2020. Technical report, CERN, 2019. (Cited on page 13.)

[38] Roberto D Peccei and Helen R Quinn. Cp conservation in the presence of instantons. *Phys. Rev. Lett*, 38(328):1440–1443, 1977. (Cited on page 13.)

[39] Roberto D Peccei and Helen R Quinn. Constraints imposed by cp conservation in the presence of pseudoparticles. *Physical Review D*, 16(6):1791, 1977. (Cited on page 13.)

[40] Zhaoyu Bai, Thomas Blackburn, Oleksandr Borysov, Oz Davidi, Anthony Hartin, Beate Heinemann, Teng Ma, Gilad Perez, Arka Santra, Yotam Soreq, et al. Luxe-npod: new physics searches with an optical dump at luxe. *arXiv preprint arXiv:2107.13554*, 2021. (Cited on page 14.)

[41] Daniel Aloni, Cristiano Fanelli, Yotam Soreq, and Mike Williams. Photoproduction of axionlike particles. *Physical Review Letters*, 123(7):071801, 2019. (Cited on page 15.)

[42] Noam Tal Hod and Arka Santra. Luxe technical note: Tracking detector. Technical report, 2023. (Cited on page 16.)

[43] Halina Abramowicz et all. Luxe technical note: Electromagnetic calorimeter. Technical report, 2023. (Cited on pages 16 and 33.)

[44] M. Bruschi et all. Luxe technical note: Scintillator screen. Technical report, 2023. (Cited on page 16.)

[45] Jenny List Louis Helary, Ruth Jacobs and Stefan Schmitt. Luxe technical note: Cherenkov detector. Technical report, 2023. (Cited on pages 16 and 17.)

[46] Kyle Fleck and Gianluca Sarri. Luxe technical note: Gamma spectrometer. Technical report, 2023. (Cited on page 17.)

[47] M. Benettoni S. Bonaldo F. Dal Corso U. Dosselli M. Giorato P. Giubilato P. Grutta S. Mattiazzo M. Morandin A. Paccagnella D. Pantano G. Simi M. Zanetti N. Cavenagh K. Fleck G. Sarri M. Skakunov A. Tyazhev A. Vinnik M. Bruschi, A. Sbrizzi and A. Zarubin. Luxe technical note: The gamma beam profiler. Technical report, 2022. (Cited on page 17.)

[48] Oleksandr Borysov Maryna Borysova and Jenny List. Luxe technical note: Backscatter calorimeter. Technical report, 2023. (Cited on page 17.)

[49] John Allison, Katsuya Amako, John Apostolakis, Pedro Arce, Makoto Asai, Tsukasa Aso, Enrico Bagli, A Bagulya, S Banerjee, GJNI Barrand, et al. Recent developments in geant4. *Nuclear instruments and methods in physics research section A: Accelerators, Spectrometers, Detectors and Associated Equipment*, 835:186–225, 2016. (Cited on pages 17 and 33.)

[50] John Allison, Katsuya Amako, JEA Apostolakis, HAAH Araujo, P Arce Dubois, MAAM Asai, GABG Barrand, RACR Capra, SACS Chauvie, RACR Chytracek, et al. Geant4 developments and applications. *IEEE Transactions on nuclear science*, 53(1):270–278, 2006. (Cited on pages 17 and 33.)

[51] Adrian Irles. Testing highly integrated components for the technological prototype of the calice siw-ecal. In *2019 IEEE Nuclear Science Symposium and Medical Imaging Conference (NSS/MIC)*, pages 1–6. IEEE, 2019. (Cited on page 18.)

[52] Omri Har-Shemesh and Antonino Di Piazza. Peak intensity measurement of relativistic lasers via nonlinear thomson scattering. *Optics Letters*, 37(8):1352–1354, 2012. (Cited on page 19.)

[53] Wenchao Yan, Colton Fruhling, Grigory Golovin, Daniel Haden, Ji Luo, Ping Zhang, Baozhen Zhao, Jun Zhang, Cheng Liu, Min Chen, et al. High-order multiphoton thomson scattering. *Nature Photonics*, 11(8):514–520, 2017. (Cited on page 19.)

[54] Olena Karacheban, Konstantin Afanaciev, Maria Hempel, Hans Henschel, Wolfgang Lange, Jessica Lynn Leonard, Itamar Levy, Wolfgang Lohmann, and S Schuwalow. Investigation of a direction sensitive sapphire detector stack at the 5 gev electron beam at desy-ii. *Journal of Instrumentation*, 10(08):P08008, 2015. (Cited on pages 21, 24, 25, and 26.)

[55] J Stone-Sundberg. Sapphire series part 1: Introduction to sapphire and synthetic sapphire, 2013. (Cited on page 22.)

[56] Daniel C Harris. A century of sapphire crystal growth: origin of the efg method. In *Optical Materials and Structures Technologies IV*, volume 7425, pages 215–226. SPIE, 2009. (Cited on pages 22 and 24.)

[57] Auguste Victor Louis Verneuil. *Mémoire sur la reproduction artificielle du rubis par fusion*. 1904. (Cited on page 22.)

[58] K Nassau and AM Broyer. Application of czochralski crystal-pulling technique to high-melting oxides. *Journal of the American Ceramic Society*, 45(10):474–478, 1962. (Cited on page 22.)

[59] J Stone-Sundberg. Sapphire series part 2: The next generation of sapphire crystal growth techniques, 2013. (Cited on pages 22, 23, 24, and 72.)

[60] Hans J Scheel. The development of crystal growth technology. *Crystal Growth Technology*, pages 1–14, 2003. (Cited on page 22.)

[61] Elena R Dobrovinskaya, Leonid A Lytvynov, and Valerian Pishchik. *Sapphire: material, manufacturing, applications*. Springer Science & Business Media, 2009. (Cited on page 22.)

[62] Maurice P Bianchi. Gallium nitride collector grid solar cell, September 10 2002. US Patent 6,447,938. (Cited on page 22.)

[63] Chandra P Khattak, Raj Shetty, C Richard Schwerdtfeger, and Saurabh Ullal. World s largest sapphire for many applications. *Journal of Crystal Growth*, 452:44–48, 2016. (Cited on page 23.)

[64] Hyoungjoon Park and H. M. Chan. A novel process for the generation of pristine sapphire surfaces. *Thin Solid Films*, 422:135–140, 2002. (Cited on page 24.)

[65] F. Bruni. Crystal growth of sapphire for substrates for high-brightness, light emitting diodes. *Crystal Research and Technology*, 50, 2015. (Cited on page 24.)

[66] MM Günther, ON Rosmej, P Tavana, M Gyrdymov, A Skobliakov, A Kantsyrev, S Zähter, NG Borisenko, A Pukhov, and NE Andreev. Forward-looking insights in laser-generated ultra-intense γ-ray and neutron sources for nuclear application and science. *Nature Communications*, 13(1):170, 2022. (Cited on page 24.)

[67] Frank Scholze, Hans Rabus, and Gerhard Ulm. Mean energy required to produce an electron-hole pair in silicon for photons of energies between 50 and 1500 ev. *Journal of Applied Physics*, 84:2926–2939, 1998. (Cited on page 25.)

[68] Feng Wang, Jie Shan, Ernst Knoesel, Mischa Bonn, and Tony F Heinz. Electronic charge transport in sapphire studied by optical-pump/thz-probe spectroscopy. In *Ultrafast Phenomena in Semiconductors and Nanostructure Materials VIII*, volume 5352, pages 216–221. SPIE, 2004. (Cited on page 25.)

[69] A Ignatenko, N Baboi, H Henschel, O Hensler, W Lange, W Lohmann, M Schmitz, K Wittenburg, and S Schuwalow. Beam halo monitor for flash and the european xfel. *proceedings of IPAC*, 2012. (Cited on page 25.)

[70] J Guo, D E Ellis, and D J Lam. First-principles calculation of the electronic structure of sapphire: Bulk states. *Physical Review, B: Condensed Matter; (United States)*. (Cited on pages 25 and 75.)

[71] Christoph E. Nebel. Bulk electronic properties of diamond, 2020. (Cited on pages 25 and 75.)

[72] Alexandr Ignatenko, Nicoleta Baboi, Hans Henschel, Olaf Hensler, Wolfgang Lange, Wolfgang Lohmann, Michael Schmitz, Sergej Schuwalow, and Kay Wittenburg. Test and first application of artificial sapphire sensors. In *IEEE Nuclear Science Symposuim & Medical Imaging Conference*, pages 650–654. IEEE, 2010. (Cited on page 26.)

[73] Julian Becker. Signal development in silicon sensors used for radiation detection, Aug 2010. (Cited on page 27.)

[74] CAEN S.p.A. Fers-5200 boards, Sep 2023. (Cited on page 27.)

[75] Yuri Venturini, Andrea Abba, Nicola Paoli, Carlo Tintori, and Massimo Venaruzzo. Fers-5200: a distributed front-end readout system for multidetector arrays. In *The 22nd International Workshop on Neutrinos from Accelerators. 6-11 Sep 2021. Cagliari*, page 166, 2022. (Cited on page 27.)

[76] WEEROC company. Scientific instrumentation sipm read-out chip. (Cited on page 28.)

[77] CAEN S.p.A. Sy5527 universal multichannel power supply system, Aug 2023. (Cited on page 31.)

[78] Simon Ramo. Currents induced by electron motion. *Proceedings of the IRE*, 27(9):584–585, 1939. (Cited on page 38.)

[79] K.S. Shah, J.C. Lund, and Frederick Olschner. Charge collection efficiency in a semiconductor radiation detector with a non-constant electric field. *Nuclear Science, IEEE Transactions on*, 37:183 – 186, 05 1990. (Cited on page 39.)

[80] Y. Nemirovsky, A. Ruzin, G. Asa, and J. Gorelik. Study of the charge collection efficiency of cdznte radiation detectors. *Journal of Electronic Materials*, 25:1221–1231, 1996. (Cited on page 39.)

[81] V S Vavilov. Physics and applications of wide bandgap semiconductors. *Physics-Uspekhi*, 37:269 – 277, 1994. (Cited on page 39.)

[82] CAEN. A5202 fers-5200 - characterization report, Feb 2024. (Cited on page 44.)